Aus der Klinik für Neurologie, Neurochirurgie und Psychiatrie –Arbeitsbereich Pädiatrische Neurochirurgie der Medizinischen Fakultät Charité – Universitätsmedizin Berlin

DISSERTATION

Magnetresonanztomographische Untersuchung der Kleinhirntonsillenmotilität bei Chiari Malformationen

Magnetic resonance imaging of dynamic cerebellar herniation in patients with Chiari Malformations

zur Erlangung des akademischen Grades
Doctor medicinae (Dr. med.)

vorgelegt der Medizinischen Fakultät
Charité – Universitätsmedizin Berlin

von
Mia Tietze
aus Berlin

Datum der Promotion: 30.11.2023

Preface

Some of the results in this work have been published in the following publication in Mai 2019:

Tietze M, Schaumann A, Thomale U, Hofmann Ph, Tietze A. Dynamic cerebellar herniation in Chiari patients during the cardiac cycle evaluated by dynamic magnetic resonance imaging. Neuroradiology. 2019 Jul;61(7):825–32.

Table of Content

List of Abbreviations

ANOVA	Analysis of variance
BOL	Basion-ophistion Line
C3-RL	Reference line as extension of upper endplate of third vertebral body
CSF	Cerebrospinal fluid
CM	Chiari Malformation
CM1	Chiari Malformation type one
CM2	Chiari Malformation type two
CM3	Chiari Malformation type three
CT	Computer tomography
FOHR	Frontal occipital horn ratio
FOHWR	Frontal occipital horn width ratio
MPRAGE	Magnetization Prepared Rapid Acquisition Gradient Echo
MRI	Magnetic Resonance Imaging
PACS	Clinical Picture Archiving System
SD	Standard deviation
VI	Visual inspection
VIDM	Voxel intensity distribution method

Abstract – English

Purpose

Cerebellar herniation can be dynamic in patients with Chiari Malformations during the cardiac cycle. Reproducible quantification of this movement could lead to better understanding of the malformation's pathophysiology and improve diagnostic criteria for Chiari patients. To automatically extract the pulsatility-dependent herniation in time-resolved MRI (CINE MRI) this work presents a voxel intensity distribution method (VIDM) and compares it to simple linear measurements. Furthermore, the extent of herniation on CINE is compared to that on static sequences, and the cerebellar movement is correlated to the presence of hydrocephalus and syringomyelia.

Methods

Using VIDM cerebellar movement in 27 Chiari patients is analyzed and results are compared to linear measurements on an image viewer (visual inspection, VI) using a paired t test. To compare the degree of herniation on static 3D MRI and CINE an ANOVA test is applied. Finally, Pearson's correlation coefficient is calculated for the correlation between presence of hydrocephalus or syringomyelia and the degree of cerebellar movement.

Results

VIDM showed tissue movement in 85% of our patients. Assuming movement ≤ 1 mm could not be detected reliably on an image viewer, movement using VI was identified in 29.6% of the patients. The difference in the detection of movement using the two methods was significant ($p = 0.002$). Herniation was greater on static sequences than on CINE in 78% of all cases, but this was not statistically significant ($p > 0.05$). The extent of cerebellar movement did not correlate with the presence of syringomyelia or hydrocephalus (Pearson's coefficient < 0.3).

Conclusions

VIDM is a sensitive method to detect tissue movement on CINE MRI and may be used to improve understanding of the pathophysiology of Chiari patients as well as objectify diagnostic criteria and indications for surgical treatment. Furthermore, VIDM could be used to evaluate e.g. cyst membranes or ventriculostomies. The missing correlation of cerebellar movement with hydrocephalus and syringomyelia in Chiari patients warrants further investigation.

Abstract – Deutsch

Zielsetzung

Kleinhirnhernierungen in Chiari-Patienten können durch die Pulsation des Liquor cerebrospinales während des Herzzyklus durch das Foramen Magnum dynamisch sein. Quantifizierung von diesen Kleinhirnbewegungen könnten das Verständnis der Pathophysiologie dieser Erkrankung verbessern sowie dazu beitragen, die Diagnosekriterien und Operationsindikationen der Chiari Malformationen reproduzierbarer werden zu lassen. Diese Arbeit stellt die Methode „Voxel Intensity Distribution Method“ (VIDM) vor, mit deren Hilfe die pulsationsabhängige Hernierung automatisch in zeitaufgelösten Magnetresonanztomographischen (MRT) Sequenzen (CINE MRT) erfasst werden kann und vergleicht diese mit einfachen linearen Messungen. Außerdem wird der Grad der Hernierung in CINE- und statischem MRT verglichen und mit der Anwesenheit von Hydrozephalus oder Syringomyelie ins Verhältnis gesetzt.

Methoden

Die Kleinhirnbewegungen in 27 Chiari-Patienten wurden mithilfe von VIDM analysiert und die Ergebnisse mit linearen Messungen auf einem image viewer (visual inspection, VI) mittels gepaarten T-test verglichen. Außerdem wurde mithilfe des ANOVA-Tests der Grad der Hernierung auf den dreidimensionalen und dynamischen MRT Bildern verglichen. Die Korrelation zwischen Kleinhirnbewegung und Vorliegen eines Hydrozephalus oder einer Syringomyelie wurde unter Zuhilfenahme des Pearson´s correlations coeffizient getestet.

Ergebnisse

Die neue Methode VIDM konnte das Vorliegen von Gewebebewegungen in 85% der Patienten zeigen. Mit der etablierten Methode VI konnte unter Berücksichtigung eines Schwellwerts von > 1 mm auf einem image viewer in 29.6% der Patienten ($p=0.002$) Bewegungen festgestellt werden. Der Grad der Hernierung war in 78% der Fälle in den statischen Sequenzen größer als in den CINE-Sequenzen, was sich statistisch jedoch nicht als signifikant zeigte ($p>0.05$). Die Kleinhirnbeweglichkeit korrelierte nicht mit dem Vorhandensein von Hydrozephalus oder Syringomyelie (Pearson‘s correlations coeffizient < 0.3).

Konklusion

VIDM ist eine sensitive Methode, um Gewebebewegungen auf der CINE MRT Sequenz nachzuweisen und könnte perspektivisch für die klinische Beurteilung und das bessere pathophysiologische Verständnis von Chiari-Patienten eingesetzt werden. Es sind darüber hinaus weitere Einsatzfelder für die Methode denkbar, beispielsweise in der Evaluation von Zystenmembranen oder Ventrikulostomien. Durch die fehlende Korrelation der Kleinhirnbeweglichkeit mit Hydrozephalus und Syringomyelie bei Chiari-Patienten eröffnen sich weitere Untersuchungsfelder.

1 Introduction

The aim of this work is to develop an objective and reproducible method to quantitatively assess movement of anatomical structures in Magnetic Resonance Imaging (MRI) and thereby enhance the understanding and facilitate the diagnosis of patients with Chiari malformations (CM). This displacement will mostly be dynamic during the cardiac cycle, which is not sufficiently detected by conventional imaging [1].

In the following the CM and their complications will be described. After a short introduction to imaging of patients with CM, a description of dynamic MRI and the difficulties arising due to the partial volume effect will be portrayed. Finally, the hypothesis of this studies expressed.

1.1 Chiari Malformations

1.1.1 Types of CM and epidemiology

The Austrian pathologist, Professor Hans Chiari, first described the CM during the 1890's as a collection of hindbrain malformations [2]. These disorders share a diminished posterior fossa and subsequent overcrowding at the craniocervical junction can lead to downward herniation of the cerebellum, brainstem compression and cerebrospinal fluid (CSF) flow abnormalities. In 1891 Chiari described the first three types of malformations adding a fourth in 1895 [3]. However, since Chiari's description of the CM, various reports across the literature do not seem to fit to the original descriptions. Therefore, new classifications have been proposed with variants of the original CM termed Chiari 0, Chiari 1.5, and Chiari 3.5 [3].

Chiari Malformations type one (CM1) is relatively common with a prevalence of approximately 1% in children [4]. According to Chiari, in these patients the tonsils lie bellow the plane of the foramen magnum. CM type 1.5 is strongly associated to CM1. In fact, it is sometimes even considered a more pronounced form of CM1, in which not only the cerebellar tonsils herniate, but also the rhombencephalon [3].

CM type 0 is defined as a syringohydromyelia that responds to craniocervical decompression surgery with no or minimal tonsillar herniation (<3 mm) [3]. CM type 0 and CM1 share clinical and some radiological aspects and as familial clustering of the two disorders is described, a genetical basis has been suggested [5].

Chiari described that in patients suffering from CM type 2 (CM2) the cerebellar vermis, brainstem, and fourth ventricle have descended caudally below the plane of the foramen

magnum [3]. CM2 is rare (prevalence of 0.4 per 1000 live births) and as children with CM2 also suffer spinal dysraphism, neurological symptoms are usually severe [4].
A synonym for the third Chiari Malformation (CM3) described by Chiari is rhombencephalocele because an osseous defect of the occipital bone occurs along with a meningoencephalocele with or without spinal involvement [4]. In a meningoencephalocele the cerebellum ± brainstem protrudes through a defect in the cranium into a sac-like swelling filled with CSF [4,6]. Although an increase in the diagnosis of CM3 has been observed as a result of fetal MRIs, CM3 is still an exceedingly rare disease and has only been reported 60 times from Chiari's first description in 1891 until 2018 [3,4]. CM type 3.5 is a variation of CM3 with an anomalous communication between neural tube and foregut [3].
Finally, the fourth type of CM presents as an occipital encephalocele through the posterior fontanel and is associated to cerebellar hypoplasia [3].
This work only includes patients with CM1 and CM2 and therefore, the following description of the diagnosis and treatment will focus on those two entities.

1.1.2 Diagnosis of Chiari Malformations

1.1.2.1 Clinical presentation

Symptoms in CM patients are caused by direct or pulsatile increased pressure at the craniocervical junction, which may result in brain stem compression and CSF flow disturbances. Medullary compression may lead to bulbar signs, such as dysphagia or dysarthria, lower cranial deficiencies, or headaches [4].
Hydrocephalus and syringomyelia are consequences of altered CSF flow, as its accumulation may dilate the central canal of the spinal cord or the intracerebral ventricles [7].
Hydrocephalus can be defined as enlargement of the ventricles in the brain due to inadequate passage of CSF from its points of productions within the cerebral ventricles to its points of absorption to systemic circulation [8]. Particularly early onset hydrocephalus prevents cerebral development causing impaired neurodevelopmental outcome with insufficient motor and sensory function as well as neurocognition [9]. If left untreated the increased intracerebral pressure causes brain damage and, in worst case, death [9].
By definition, all children with CM2 have an additional spinal dysraphism. Children with CM2 are usually diagnosed prenatally by ultrasound or immediately postnatally [10]. Patients with CM1, however, often remain asymptomatic for many years and may then present with vague symptoms such as headache or neck pain [4], making the diagnosis more challenging.

1.1.2.2 Imaging of patients with CM

Imaging has become a vital part of the diagnostics of CM. It is usually achieved by ultrasound in young infants and MRI or Computertomography (CT) when the fontanelle is closed. CT presents better illustration of bony structures, shorter duration and lower costs than MRI. Despite these benefits, the high radiation exposure of this technique and poor resolution of soft tissue makes it inferior to MRI.

CM1 and CM2 are diagnosed by determining the herniation, i.e. downward displacement, of the cerebellar tonsils [4]. Defining the cutoff value for this herniation is tricky, as the position of the tonsils follows a normal distribution within healthy controls [1]. CM patients may present with little herniation and symptoms, or no symptoms but significant herniation [1]. Despite this, currently a CM is diagnosed when patients present with tonsillar position is > 5 mm below a line connecting the basion with the opisthion (BOL) on conventional sagittal brain images and show associated clinical symptoms [4]. However, the evaluation of symptoms is susceptible to subjectivity and it turns out that the determination of the tonsillar position is also inconsistent. First, like all bony structures, the basion and ophistion can be difficult to visualize in MRI and if the patient has been treated surgically, the antomical landmarks may be missing [11]. Second, determining the tonsillar position shows high degree of variability even among experts [1]. Lawrence et al. assessed the interrater fluctuation among seven expert in 2018, finding wide-ranging results and 6.0% false positive and 11.7% false negative diagnosis [1]. According to Lawrence et al., in 2007 11.000 CM1 patients were treated in the US and only 20-40% of patients were reported to experience improvement of symptoms. This reflects the imperative need for objective, reproducible diagnostic criteria to better recognize patients. Improved diagnostic should thereby lead to the prevention of complications in patients and the stopping unnecessary surgeries. As possible solutions, Lawrence et al. propose machine learning and the analysis of dynamic processes within the posterior fossa as diagnostic criteria [1] and we have attempted to partly address this in our work.

1.1.2.2.1 Dynamic Imaging

Dynamic processes (flow, thin obstructing membranes, or intermittently obstructing brain structures) cannot be captured using conventional MRI sequences. To analyze dynamic processes in MRI different methods have been described, whereof the following two are the most common. The first method is the use of flow-sensitive phase contrast MRI, which is a

technique that allows the evaluation and quantification of flow-dependent, physiological processes, i.e. the flow of blood or CSF [12]. The achievement of flow sensitive MRI is usually at the expense of anatomical detail. The second method is the use of steady-state free precision MRI, which is a technique for the evaluation of dynamic processes with acceptable morphological accuracy. It is a cardiac-gated, dynamic 2 dimensional (2D) sequence that has been termed CINE [13,14]. The CINE sequence has been developed for the visualization of cardiac function and is currently the gold standard for the non-invasive assessment of cardiac ventricular function and wall motion [15]. In this study, we use the CINE sequence to evaluate dynamic tissue herniation in Chiari patients, as the degree of herniation as well as the pulsatile mobility might influence the development of complications and symptoms.
Sharma et al. investigated inter- and intra-observer assessment of tonsillar pulsatility in cardiac gated MRI sequences of Chiari patients [16]. In their study, two experienced neuroradiologists analyzed the movement of the cerebellar tissue in 44 patients (33 CM1, 2 CM2 patients and 7 other diseases as well as 5 patients with headache). They used the inbuilt measuring tool on their clinical picture archiving system (PACS) to assess the dynamics. A scale from 0 to 2 (in which 0 was no movement, 1 was minimal movement, and 2 marked movement) was developed for a qualitative evaluation. While the intra-observer agreement was almost perfect, disagreements between the observers were substantial. As limitation to their study, Sharma et al. discuss the difficulties in finding the margin of the cerebellar tissue due to partial volume effects (see point 1.2) [16].
Cousin et al. suggest a possible method for the analysis of motion is a pixel shift program (3). However, their description of the method was very limited and thus unfortunately not reproducible.

1.1.2.2.2 Imaging of patients with hydrocephalus

Imaging of patients with hydrocephalus is pivotal to diagnose and monitor disease. Different indices to quantify ventricular dilatation have been described [17]. During the late 1990's O'Hayon described the frontal and occipital horn ratio (FOHR) in children with ventriculomegaly that has since been used in the clinical and research context [18]. According to O'Hayon, the children have a hydrocephalus when the FOHR ≤ 0.37 [19]. While volumetric measurements are more precise [19] the simplicity of the FOHR makes it a valuable and easily applicable tool in research and clinical settings. However, as the FOHR measures the span of the anterior and posterior parts of the ventricles, small or asymmetric ventricles are not reliably assessed. Therefore, Jamous et al. developed the frontal and

occipital horn width ratio (FOHWR) in 2003 measuring the width of each ventricle [20]. While the FOHWR is the better measurement for small and asymmetric ventricles, the FOHR is easier applicable, and more widely used. Both linear measurements show good linear correlation to volumetric volumes [20] and we decided to use the FOHR in this study.

1.1.3 Treatment of patients with Chiari Malformations

Craniocervical decompression is the only effective treatment for patients with CM [3]. The aim is to prevent further complications, relieve symptoms, and allow cerebral development. Therefore, a normalization of the CSF flow is important [21]. The operation involves an occipital craniectomy at the posterior aspect of the foramen magnum, the removval of the posterior arch of the atlas, a dural incision, and optionally a duraplasty, lysis of arachnoid adhesions or even resection of the tonsils [3,22]. Possible complications, such as leakage of CSF or consequtive meningitis may be detrimental. It is therefore vital, that every surgeon evaluates indications for a cranio cervical decompressionion and that the neccessity for a duraplasty would possibly be supported by objective diagnostic tools.
In a study performed by Radmanesh et al., three independent radiologists with different degrees of experience evaluated movement of cerebellar tonsils in 22 CM1 patients. On a cardiac gated dynamic sequence, movement was analyzed semi-qualitatively and quantitatively before and after craniocervical decompression [13]. For a semi-quantitative exploration, movement was measured using the inbuilt measuring tool of their PACS with the scale from 0 to 2 that had also been used by Sharma et al (see point 1.1.2.2.1). They concluded, that movement decreases considerably after the neurosurgical intervention and that the quantitative assessment is more reproducible than the qualitative [13].

1.2 MRI and the partial volume effect

One important issue that affects cross-sectional imaging in general is the partial volume effect, i.e. the averaging of different structures in a data volume. In MRI, continuous data is sampled in a grid of discrete voxels, which are three-dimensional units containing the imaging data. If only one type of tissue is represented within one voxel, that voxel will show an intensity characteristic for this type of tissue. However, in the case of a voxel containing several types of tissue, its intensity will be a combination of all tissue intensities occurring within this voxel. From this it follows that ultimately all intensities in a voxel are averaged or blurred. Usually, this poses a problem for the visualization of very delicate structures as thin

membranes or for borders between two discrete tissue types and is aggravated in low-resolution imaging data. This concept is described as the partial volume effect in literature [23] and is visualized in Fig. 1 for the MPRAGE sequence in which one voxel has the dimensions of 0.9 mm ∗ 0.9 mm ∗ 0.9 mm. In Fig. 1a, a single type of tissue is represented within the voxel (in reality only white in color) and, thus, the intensity in the reconstructed MRI voxel reflects the tissue correctly (white). In Fig. 1b, however, two different tissue types are contained within the voxel (white and dark grey in reality) and therefore signal intensities in the reconstructed voxel are a combination of the two tissue types (light grey).

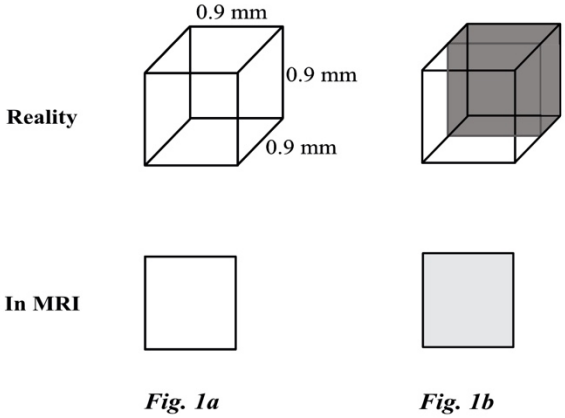

Fig. 1a *Fig. 1b*

Fig. 1 Partial volume effect in the MPRAGE sequence in which a voxel measures 0.9 mm ∗ 0.9 mm ∗ 0.9 mm. **Fig. 1a** only one type of tissue in the voxel and hence the MRI reflects the intensity of this tissue. **Fig. 1b** two different types of tissue within the voxel and therefore MRI is a combination of the two intensities.

In order to analyze volumes and structures in MRI objectively one has to be aware of the partial volume effect. In the case of CM patients, it becomes important when determining the border between the cerebellar tonsils and the CSF, especially when analyzing the relatively large voxels of the CINE sequence ($1 * 1 * 4$ mm^3). Images are intrinsically noisy due to the sampling of continuous data and when analyzing images one need to take error bounds into account [23].

1.3 Hypothesis of this study

a) The herniation of the cerebellar tonsils in CM patients is dynamic due to the CSF and tissue pulsatility. This can be assessed on MRI and quantified objectively as a reliable and easily reproducible mean.
b) The degree of herniation is different on dynamic and conventional, static MRI, respectively.
c) CM patients with a stenosis in the foramen magnum due to cerebellar herniation have a higher risk of hydrocephalus owing CSF flow disturbances.

2 Methods

2.1 Patients

The CINE sequence became part of our standard procedure for Chiari patients in January 2016. Therefore, we identified all MRI examinations including a CINE sequence from January 2016 to July 2018. Imaging had been requested for different reasons, such as follow-up exams of known C1M and C2M, craniosynostosis, or clinical symptoms that could be caused by cerebellar or brainstem compression. In total 81 MRI examinations were identified. In 36/81 a cerebellar herniation could be detected on the static and/or on the dynamic MRI sequence. Due to severe artifacts we had to exclude 6 cases and in 3 cases the foramen magnum was so overcrowded by cerebellar and brainstem tissue that no movement could be observed so that further analysis for dynamics did not appear useful. Twenty-seven patients remained of whom 4 had been diagnosed with CM2 (14.8%), 10 with CM1 (37%), and 10 patients had secondary herniated cerebellar tissue in simple or complex craniosynostosis conditions (37%). Thirteen boys and 14 girls were included. The mean age was 8.45 (standard deviation, SD, ±5.32 years).

2.2 MRI-Data

All MRIs had been obtained on a 3T MRI-System (Siemens Magnetom Skyra, Erlangen, Germany) with a 64-element head/neck coil. To ensure minimal movement the heads of the patient had been fixed by cushions. All children were provided with hearing protection. Scans included a static series (either 3D T1-weighted gradient echo, sagittal MPRAGE, with a voxel size of $0.9 * 0.9 * 0.9\ mm^3$ or a 3D T2-weighted TSE sequence, sagittal T2SPACE, with a voxel size of $0.5 * 0.5 * 0.5\ mm^3$) and a pulse triggered, single slice CINE sequence (True Fast Imaging Steady State Precession, TrueFISP) with a voxel size of $1 * 1 * 4\ mm^3$. Twenty-two of the CINE sequences included 128 time frames in one cycle and the individual images measured $240 * 240$ voxels. In five cases the images measured $210 * 208$ voxels and the loop consisted of 125 time frames (three cases) or 16 time frames (two cases).

2.3 Quantifying dynamic tonsillar/vermis displacement by voxel intensity distribution method, VIDM

Displacement is defined as the change in location of one point over time. Therefore, to evaluate displacement, one needs to define an exact point. When analyzing the tonsillar/vermis displacement in the CINE sequence an obvious choice is the point of

intersection between the cerebellum and the CSF. As the cerebellum is hypointense (grey) in the CINE sequence and the CSF hyperintense (white), one would expect the progression from cerebellum to CSF to be a clear transition from grey to white. Fig. 3a shows a typical image form a CINE sequence with fig. 3b being a magnification of the herniated tissue [24].
Due to the slice thickness in the CINE sequence (4 mm compared to 0.9 mm in the 3D MPRAGE sequence) partial volume effects play a significant role for the analysis. Fig. 3b demonstrates how at least 8 voxels show various shades of grey rather than a clear margin from white to grey. As the tonsillar/vermis displacement in the sequence is only a few millimeters, while the in-plane dimension of the voxels is 1 mm, a far more accurate localization of the intersection point is required.
In order to solve this problem, we developed a method to define a precise reference point in the transition and observe its change in position over time. The point with the highest contrast in MRI-intensity between one voxel and its neighboring voxel was chosen. The method was implemented using the scripting language of the Igor Pro (WaveMetrics, Lake Oswego, OR 97035, USA) data analysis software. To perform the analysis, it was necessary to reformat the CINE movies from movie files (.mov) into separate frames (.tif). No information was lost in this process.

For each patient, the following steps were executed by the author using the software program:

1) *Importing data into the software*
   All frames in a sequence were imported into the software according to their individual sizes.
2) *Finding area of interest*
   From the data set of each patient, a region of interest similar to Fig. 3b was identified.

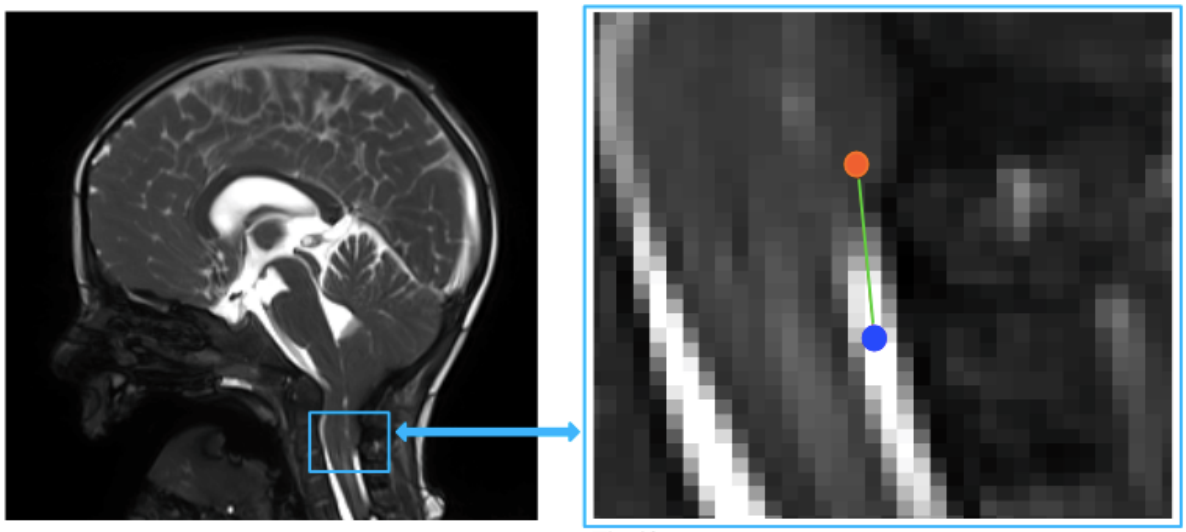

Fig. 3a *Fig. 3b*

Fig. 3a CINE sequence of a patient with a Chiari Malformation. **Fig. 3b** Magnification of the tonsillar region and MRI-intensity profile line from the tonsils (orange point) to the cerebrospinal fluid (blue point). Adapted from Fig. 1 from Tietze et al. (24).

3) *Placement of the MRI-intensity profile line*

On an arbitrary image in the sequence, a line was drawn from one point to another. The position of the first point was selected so it was clearly set within the cerebellar tissue (grey color) and the position of the second point was chosen so it was within the CSF (white color). In the example shown in fig. 3b the defined line is 12 voxels long. Note that the choice of the image within the frame sequence is irrelevant, as only relative changes are of interest.

4) *MRI-Intensity-extraction for all frames, I(x)*

The intensities, i.e. the greyscale values, of all voxels crossed by the MRI-intensity profile line were extracted automatically for all frames in the sequence. Fig. 4b shows such a complete data set, i.e. the intensity along the line for all frames in the sequence. The time-dependence measured in frames is plotted along the y-axis (y=128 frames) and the position on the line is given along the x-axis in units of voxels. Fig. 4c shows two cuts through this two-dimensional data set: the position-dependent intensity along the MRI-intensity profile line for two time points. The first time point plotted is at t=50 (dashed, blue line), in which the tonsils are positioned cranially. The second time point displayed is at t=100 (solid orange line), in which the tonsil's position is further caudal.

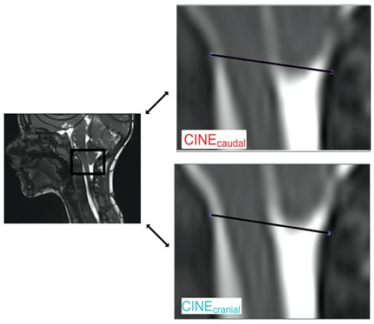

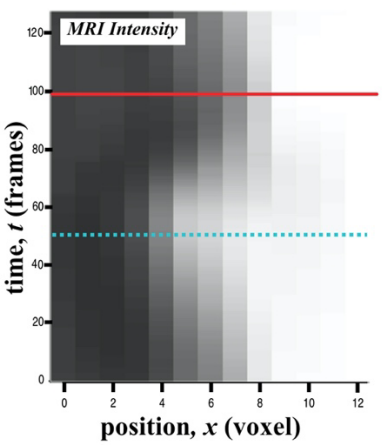

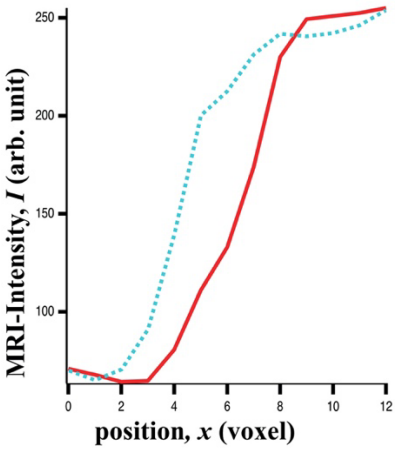

Fig. 4a *Fig. 4b* *Fig. 4c*

Fig. 4a A CINE sequence with two images at different time points (t=100 and t=50) within one sequence have been magnified. The position of the placed black line does not change and it can be seen that the tonsil move from caudal (upper image) to cranial (lower image). The same can be seen in **Fig. 4b** showing MRI-intensities change along a defined MRI-intensity profile line of 12 voxel (x-axis) for the 128 frames (y-axis) of one single CINE sequence. The orange solid line is at t=100 and corresponds to the $CINE_{caudal}$ in fig. 4a. The dashed blue line at t=50 corresponds to $CINE_{cranial}$ in fig. 4a. **Fig. 4c** MRI-intensity in an arbitrary unit (y-axis) has been extracted for the two time points. The solid orange line shows the intensity at t=100 and the dashed blue line at t=50 of Fig. 4b. Fig. 4c has been adapted from Fig. 1 in Tietze et al. (24).

5) *Determining the change in intensity per frame, dI(x)/dx*

The point in which the contrast from one voxel to the adjacent is the highest is also the point in *I(x)*, where the slope is the steepest. Fig. 5a shows the 1st derivative of the intensity at the position (*dI/dx)* as its maximum corresponds to the point where the gradient is the steepest. The software automatically creates a curve of the respective first derivative of the MRI-intensity curve, *dI/dx,* for all frames in the sequence. In fig. 5a two of these MRI-intensity curves are displayed, similarly to fig. 4. The first MRI-intensity line (dashed and blue) is the line for the time frame t=50. The second (solid and orange) line is the line from time frame t=100. Fig. 5b shows the result for an entire sequence in the same way as fig. 4b, with the time along the y-axis and the position in voxel on the x-axis. The difference to fig. 4c is that fig. 5b shows the color coded first derivative of the intensity instead of the intensity as such. The color-coding ranges from blue to red with the maximum of changes in MRI intensity being red. Note that this representation of the data shows a clear displacement of the maximum by up to 4 voxels over the time series in the presented case. The representation using the derivative renders the effect more evident and quantifiable compared to figure 4b.

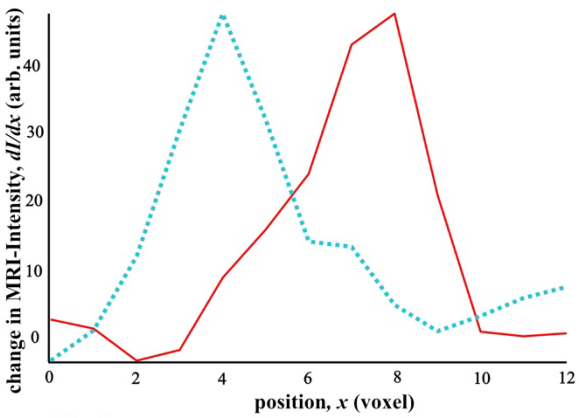

Fig. 5a

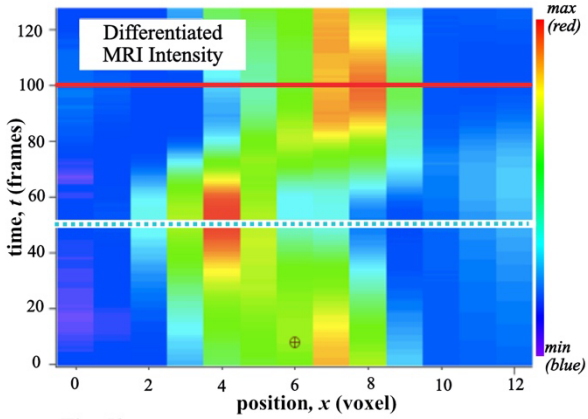

Fig. 5b

Fig. 5a Change in MRI-intensity, *dI/dx*, on the previously defined MRI-intensity profile line. The dashed blue line is at time frame t=50 and the solid orange line is at t=100. **Fig. 5b** Change in MRI-intensity for all frames. The red colour indicates a maximum of *dI/dx.* The solid orange line drawn at t=100 is equivalent to the solid orange line in fig. 5a. Similarly, the dashed black line is equivalent to the dashed blue line in fig. 5a (for color version see electronic form). Adapted from Fig. 1 in Tietze et al. (24).

6) *Quantifying the displacement using the absolute maximum of dI/dx*

The displacement was now defined as the difference in position of the maxima in the 128 time frames of *dI(x)/dx* for each patient.

Equation 1

$$displacement = x_1 - x_2$$

In the example provided in Fig. 5b, the widest spread is between time frame t=50 in position x=4 (dashed blue line in figures 4 and 5) and in time frame t=100 in position x=8 (solid orange line in figures 4 and 5). Hence, total displacement between these two timeframes must be 4 voxels (8-4 voxels). Due to measurements of a continuous movement at defined time points, uncertainties arise (described in fig. 6 in more detail). If the uncertainty for the position of the first maximum is σ_1 and the uncertainty of the second maximum is σ_2 the total uncertainty, σ_{tot}, is calculated according to gaussian uncertainty propagation as follows

Equation 2

$$\sigma_{tot} = \sqrt{\sigma_1^2 + \sigma_2^2}$$

The position of the maxima can only be determined with an uncertainty of at least ±1 voxel, since it is measured in integer voxel values. Hence, σ_{tot} is given by

$$\sigma_{tot} = \sqrt{1^2 + 1^2} = 1.4$$

A significant movement can only be identified for a displacement exceeding 3 times σ_{tot} and thus > 4.2 voxels. Actually, displacements of more than 4 voxels are very rarely observed in our data (the example given in Fig. 3-5 is actually showing a large displacement for illustrative purposes). Indeed, when following this strict requirement, detection of movement cannot be claimed by any cases.

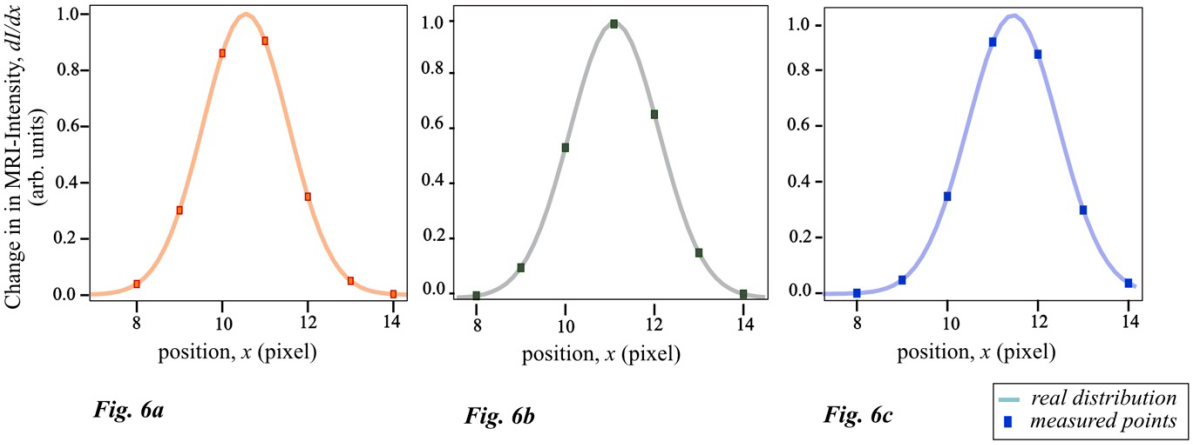

Fig. 6a *Fig. 6b* *Fig. 6c*

Fig. 6 Cases in which discrete points are used to display a real distribution. As measurements are only conducted at certain time points they cannot adequately illustrate the real distribution. In all three cases the measured maximum is at position x=11, although this is only true for Fig 6b. **Fig. 6a** real maximum = 10.55. **Fig. 6b** real maximum = 11.0. In **Fig. 6c** real maximum = 11.45.

As it turns out, merely using the maximum of changes in MRI intensity is a poor method to measure the displacement. Not only are the uncertainties large, the approach also makes little use of the available data since it only considers a single data point with the highest gradient. This issue is demonstrated in Fig. 6 which illustrates three cases in which a hypothetical real distribution (smooth line) is sampled at discrete points of x (squares). In all three cases, the point at x=11 is the measured maximum but the true maximum of the distribution varies between 10.55 in Fig. 6a and 11.45 in Fig. 6c. This confirms not only that using just the maximum value for the discrete sampling induces a relevant uncertainty, it also illustrates that e.g. estimating the position of the distributions maximum using information of the highest point and the points to its left and right might deliver more accurate results.

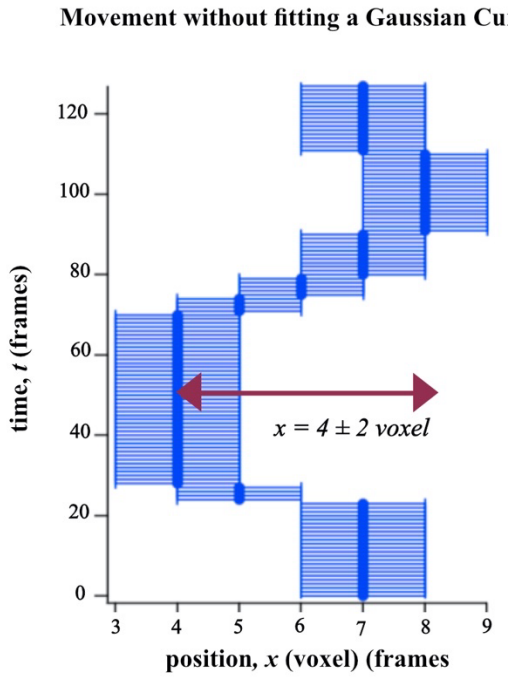

Fig. 7a

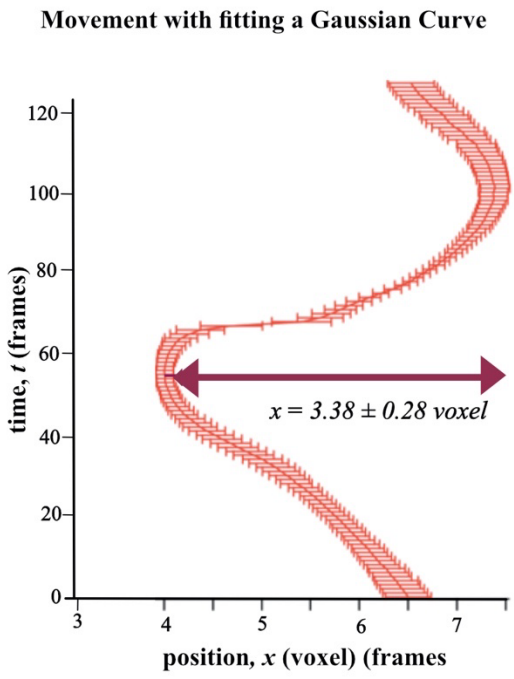

Fig. 7b

Fig. 7a Change in position of the maximum of the derivative of the MRI-intensity depending on the time in frames obtained from tracking the maximum position in *dI/dx*. **Fig. 7b** Maximum of the derivative has been determined by a fit to a Gaussian curve, which enables values to be measured more precisely. Adapted from Fig. 1 in Tietze et al. (24).

7) *Quantifying the displacement by fitting to a Gaussian curve*

The large uncertainty in the determination of the displacement discussed in the previous section can be decreased by fitting a Gaussian curve to *dI(x)/dx.* The choice of a Gaussian is not critical – it is just a simple curve with a maximum and Gaussian broadening of a sharp edge would also be expected in many resolution-limited techniques [25]. By fitting the entire distribution with a Gaussian, not only one point is taken into account, but the entire data set. Movement is measured as in Equation 1. Using this approach, uncertainties depend on how well the curve can be fitted to all existing data points. Hence, each time-dependent position has individually calculated uncertainties.

Fig. 7a illustrates the displacement of 4±2 voxels for the exemplary patient in fig. 3-5 as obtained from the maximum in *dI/dx*. Fig. 7b shows the displacement for the same patient obtained by the same method in addition to a Gaussian fit. Here, only 3.38 voxels of displacement are measured, but a greatly reduced uncertainty of only ± 0.28 voxels.

In accordance to the three-sigma rule, displacement is defined to be significant, when it exceeds 3 σ_{tot} calculated from the two individual uncertainties as in Equation 2.

This ensures that displacement is only recognized when the probability of it being greater than uncertainties in measurements is 99.7 % [26].

8) *Conversion from voxel to millimeters*
   Finally, all results were converted from the unit of voxels to a unit of mm. In the CINE sequence one voxel is approximately $1 * 1 * 4\ \mathrm{mm}^3$ (the 4 mm refer to the thickness of the slice). Therefore, the displacement in voxel corresponds to the displacement in mm. In the example of Fig. 7 this would be 3.38 ± 0.28 mm.

2.4 Visual Inspection, VI

The visual inspection of the static, sagittal MRI images (MPRAGE) and the CINE sequence images was preformed using the open source software HOROS (Horosproject.org; Nimble Co LLC d/b/a Purview, Annapolis, MD, USA). All images were analyzed in a 5 times magnification to ensure precision. In order to account for errors due to patient movement, static images were resliced to match the CINE sequence and the anatomical plane. This was controlled by the cross-reference lines in HOROS.

The common quantification for the extent of cerebellar herniation is the distance between the most caudal point of the tonsils and the line connecting the basion with the opisthion (BOL). For many aspects of this study, however, we were unable to use the BOL as a reliable marker, because bony structures are very poorly visible in the heavily T2-weighted CINE sequence. Moreover, four of the patients had been treated with a craniocervical decompression and, hence, no BOL could be defined. A method using the perpendicular line set in HOROS was developed. For this method, a reference line (RL) was drawn as an extension of the upper endplate of the third vertebral body C3. Fig 8a-c shows an example in which C3-RL is the line from c to a. A perpendicular line to C3-RL was drawn to

a) the tonsils in the static, MPRAGE MRI sequence (Fig. 8a)
b) the most cranial ($\mathrm{CINE}_{\mathrm{cranial}}$, Fig. 8b) point of cerebellar tissue in the CINE sequence
c) the most caudal point ($\mathrm{CINE}_{\mathrm{caudal}}$, Fig. 8c) of the cerebellar tissue in the CINE sequence

The copy-paste function was used to ensure the exact same position and inclination of C3-RL.

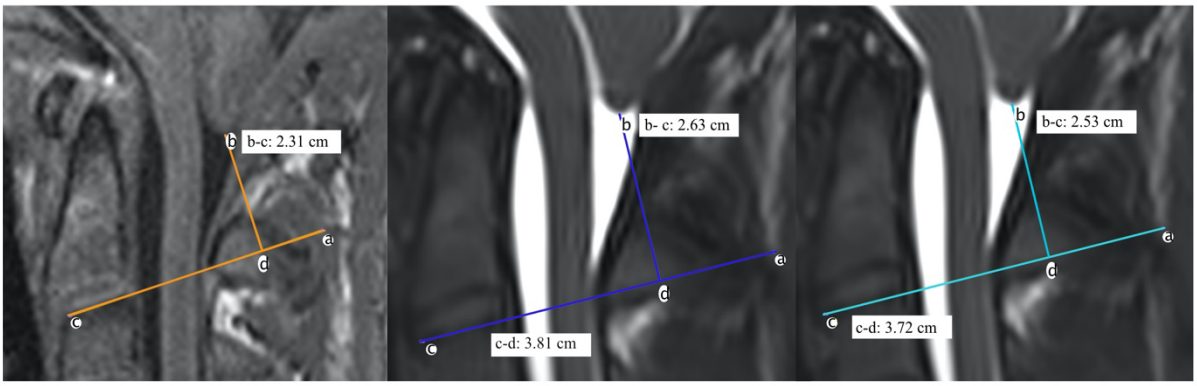

Fig. 8a *Fig. 8b* *Fig. 8c*

Fig. 8a Static, sagittal MPRAGE image. The reference line from c to a was drawn as an extension of the upper plate of the third vertebral body (C3-RL). Perpendicular to C3-RL, the line from b to d measures the distance to the herniated cerebellum. **Fig. 8b-c** CINE sequence. **Fig. 8b** $CINE_{cranial}$, **Fig. 8c** $CINE_{caudal}$. Adapted from Fig. 2 in Tietze et al. (24).

The distances between all points in the perpendicular line set were collected and used to calculate the movement of the cerebellar tissue in two different dimensions:

1. **Cranio-caudal movement (CC)**

   The distance between point b and d in the perpendicular line set changes as the cerebellar tissues moves from cranial to caudal. It can be quantified by subtracting the length of the line bd in $CINE_{cranial}$ from the length of line bd in $CINE_{caudal}$. In the example in Fig. 8, the cc distance would be

   $$CC - movement = CINE_{cranial} - CINE_{caudal} = 2.63 - 2.53 = 0.10\,mm$$

2. **Anterior-posterior movement (AP)**

   C3-RL is constant, but the point of intersection (d) with the line bd changes. When calculating the change in length from c to d may be equivalent to an AP-movement. The following example is from the patient in Fig. 8

   $$AP - movement = \Delta length\ of\ line\ cd = 3.81 - 3.72 = 0.09\,mm$$

2.5 Frontal and Occipital Horn Ratio (FOHR)

For the FOHR calculation the sagittal MPRAGE was reformatted to axial series using HOROS. To ensure that the angulation of the axial slices was identical in all patients, reformations were made parallel to the undersurface of the corpus callosum as shown in fig. 9. The FOHR was calculated according to O'Hayon [19] using the following equation

$$FOHR = \frac{distance\ between\ frontal\ horns + distance\ between\ occiptal\ horns}{2 * biparietal\ diameter} = \frac{A + B}{2C}$$

Fig. 9 shows a reformatted, axial MPRAGE slice and demonstrates an example of a hydrocephalic case with an FOHR > 0.37.

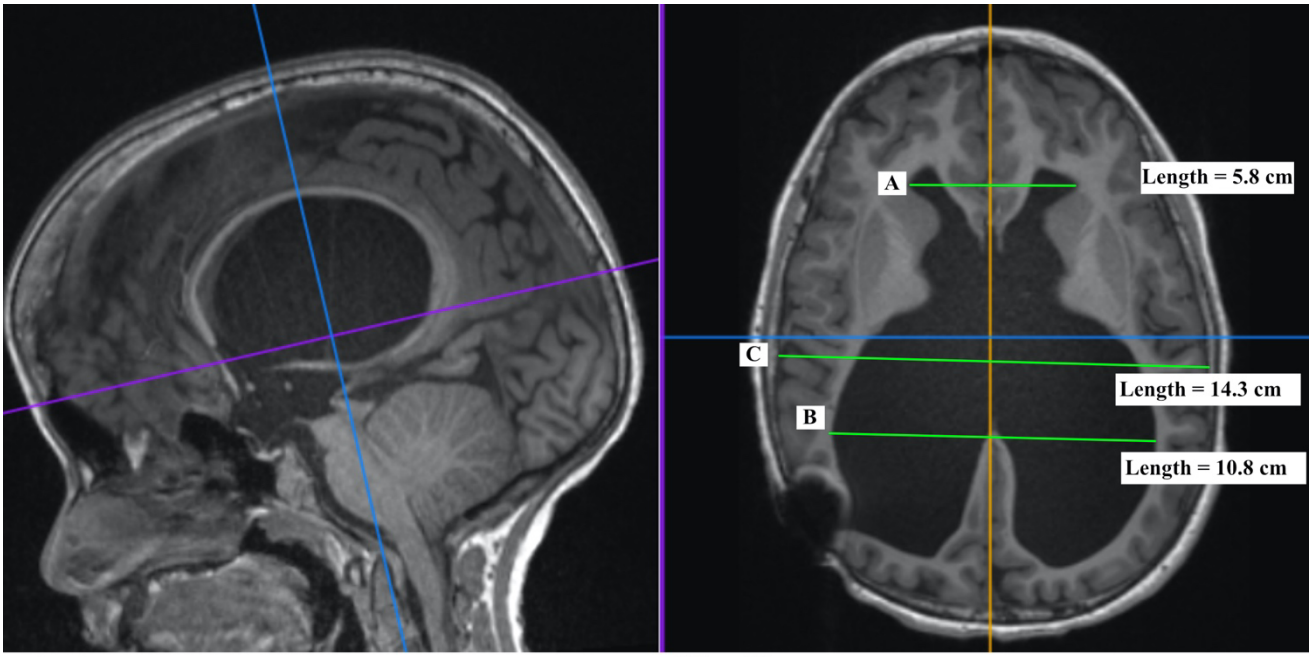

Fig. 9a *Fig. 9b*

Fig. 9 Reformatted MPRAGE image of a 10-year-old child with a Chiari Malformation type two. The sagittal image (Fig. 9a) shows the angulation of the axial slice (Fig. 9b). The frontal and occipital horn ratio is measured on the axial image with A being the distance between the frontal horns, B the distance between the maximal extent of the occipital horns, and c the biparietal diameter. In this case the Frontal and Occipital Horn Ratio is 0.58 and thus hydrocephalic.

2.6 Statistical Analysis

Statistical analysis was preformed using the open source program R (R Foundation for Statistical Computing, Vienna, Austria. http://www.R-project.org/). Mean values are given together with standard deviation (SD). Boxplots and a paired t-test were used for comparison (α=0.05). Cohen's d was calculated to find whether the difference in mean in the two different methods was significant. The adjusted R^2 test was used to analyze regression. An ANOVA test was used to determine whether there was a significant difference in herniations on the static image and dynamic sequence. Cohen's kappa was used to determine interrater agreement in the VI.

3 Results

3.1 Comparison of dynamic cerebellar displacement in the CINE sequence using the voxel intensity distribution method and visual inspection

The VIDM that took only one point into account did not reveal tonsil movement in any patient due to the large uncertainties of the approach. Therefore, the following only refers to the analysis based on a Gaussian curve adaptation method.

A displacement of the CSF-cerebellum interface between 0.14 ± 0.11 mm and 3.38 ± 0.16 mm was detected during the CINE loop (mean 1.34 mm; SD ± 0.93 mm). Further details on the obtained data is summarized in table 2. Fig. 10 shows a boxplot comparing the VIDM to VI. The movement detected using VIDM was significantly larger than VI ($p=0.002$; Cohen's d 1.54). In agreement with our definition of a detectable displacement in VIDM ($CINE_{cranial} - CINE_{caudaul}$) ≥ 3 SD, 22/27 patients showed tonsillar/vermis displacement during the cardiac cycle. Assuming that a movement less than 1 mm cannot be detected reliably in VI, only 8/27 patients showed movement using linear measurements in a clinical image viewer.

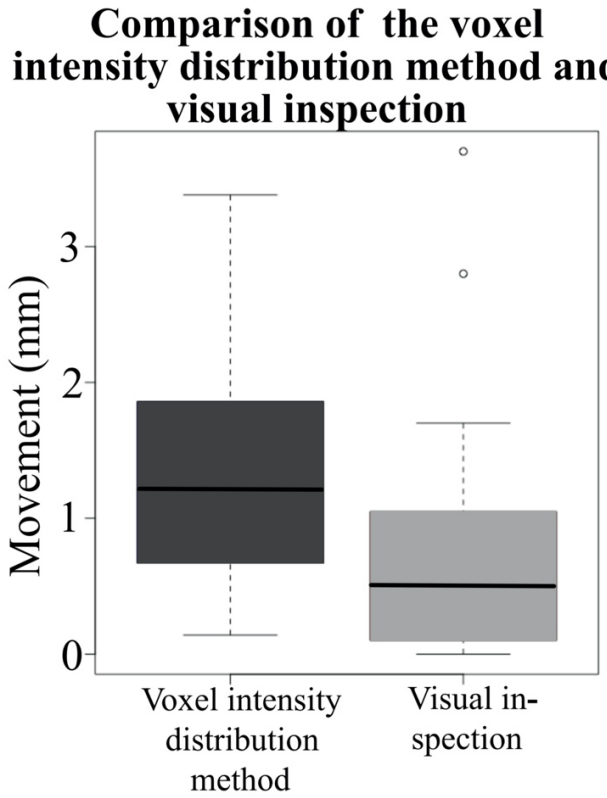

Fig. 10

Fig. 10 Boxplot comparing the tonsillar/vermis movement in the CINE sequence using the voxel intensity distribution method (darker grey on the left) and visual inspection (lighter grey on the right). The boxplots show that movement using the voxel intensity distribution method detects significantly larger displacements than the visual inspection. The median is given by the line, and the whiskers indicate 1.5 ∗ the interquartile range. Adapted from Fig. 3 in Tietze et al. (24).

3.2 Movement detected by visual inspection

3.2.1 Movement in the craniocaudal direction

Craniocaudal displacement ranged from 0 to 4 mm (mean 1 mm; SD ± 1). In 7 patients, no movement was found.

Fig.11 illustrates the correlation between the degree of herniation of the cerebellar tonsils/vermis (measured as the distance between cerebellum-CSF interface and BOL) and the CC dynamic displacement (VIDM method). The describing adjusted R^2 value of 9% indicates a poor relationship (p=0.06).

Please note that Fig. 11 also shows that all four patients with CM2 (indicated by dark grey) neither moved in the AP nor CC direction. Hence, all detected dynamic displacements (AP and CC) were in CM1 patients.

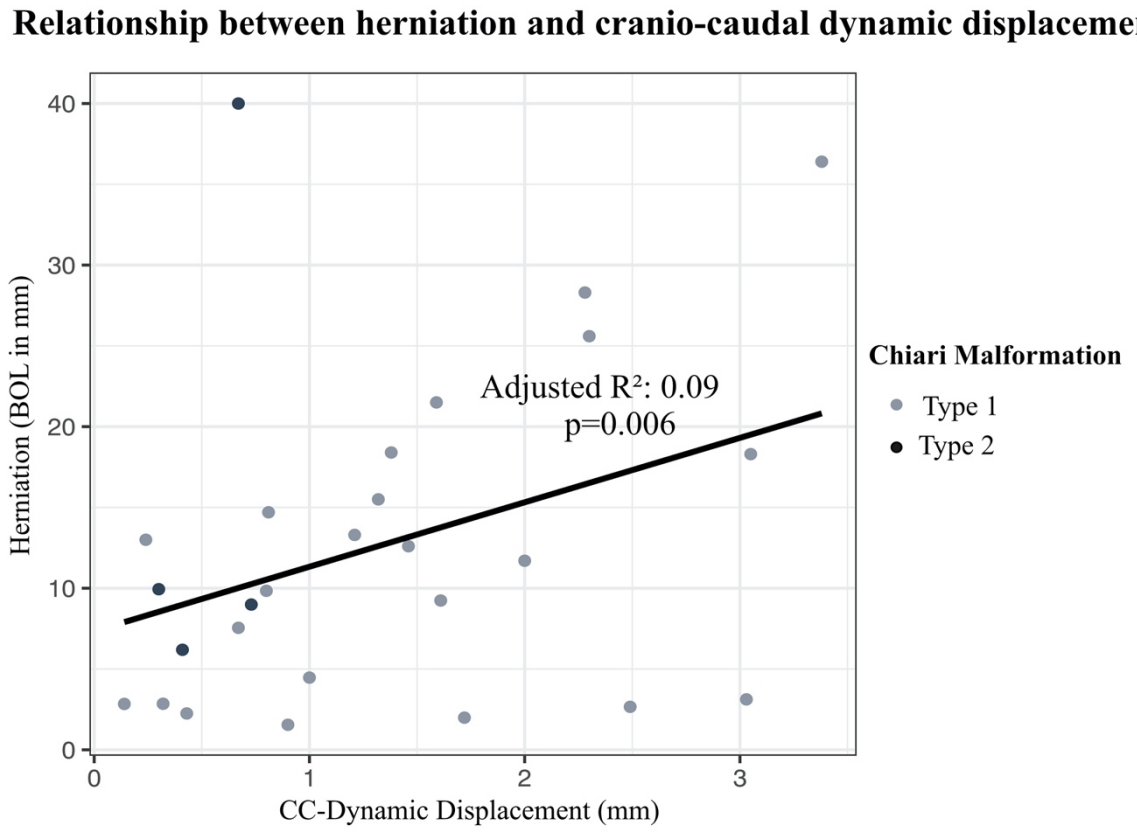

Fig. 11

Fig. 11: Correlation between the degree of herniation measured as the distance from the Basion Opisthion Line (BOL) to the cerebellum-CSF interface and the cranio-caudal (CC) dynamic cerebellar displacement. Patients with Chiari Malformation type 1 are indicated by light grey points (n=23) and type 2 by dark grey points (n=4). Orange markers indicate no movement (n=7) in the CC direction

3.2.2 Movement in the antero-posterior direction

Antero-posterior (AP) displacement ranged from 0 to 2 mm (mean 1 mm, SD ± 1 mm; Fig. 12). In 5 patients, no movement was found.

In 9/27 patients, movement ≥1 mm in the AP direction was observed, where the herniated cerebellar tissue moved anteriorly (towards the medulla oblongata) during caudal displacement. Fig. 12a shows the lack of relationship between the extent of herniation (measured as distance from BOL) with the AP-movement with an adjusted R^2 of 4% and a p-value > 0.05. In two cases, the tissue moved posteriorly, thus showing the AP movement in fig. 12a and 12b being negative. Six of the nine cases only showed AP and no CC movement. Fig. 12b shows no correlation between the AP and CC movement with an adjusted R^2 of 0 % and a p-value > 0.05.

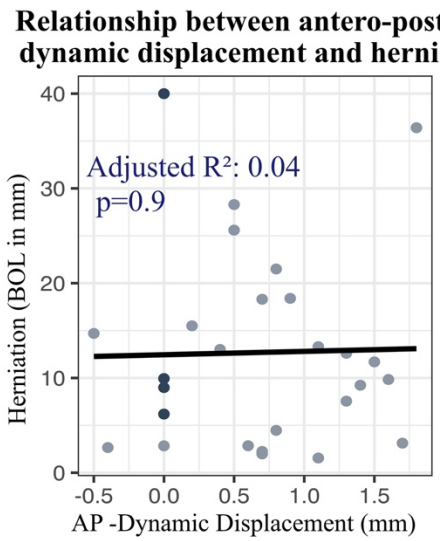

Fig. 12a

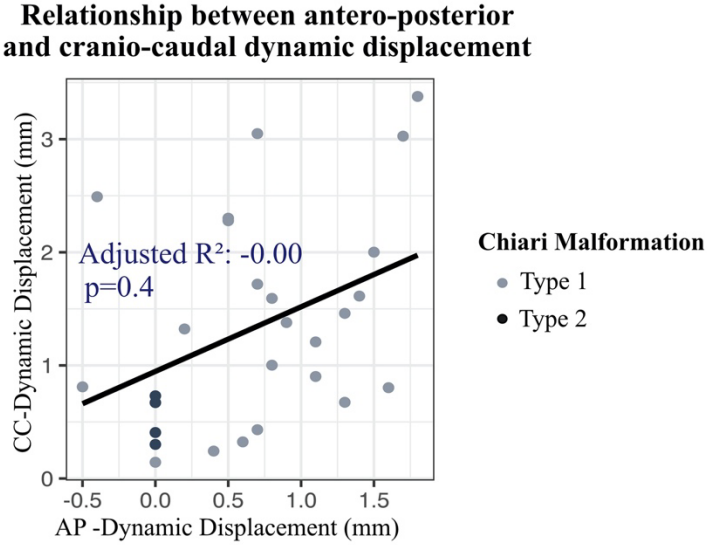

Fig. 12b

Fig. 12a: Correnation between the antero-posterior (AP) movement and the herniation from the BOL. Note that movement is only shown in patients with Chiari Malformation type 1. Five cases show no movement at all. **Fig. 12b**: Correlation between the AP and CC movement. Regression is indicated by adjusted R^2 and p-values.

3.3 Relationship between spinal cord pathologies and dynamic cerebellar displacement

In 3 of the 27 patients a dilation of the central canal was found. The first patient had a syringohydromyelia of 7 mm at the height of TH6, the second had a dilation less than 2 mm from C3 to TH12, and the third of 3 mm from C3 to C5. Two patients had significant edema in the cervical spinal cord at the height of C3 and between C2 and C4 cord. Thus, 5/27 patients showed a spinal cord pathology (19%). The mean movement of patients with a spinal

cord pathology was 1.82 mm compared to a mean movement of the patients without a spinal cord pathology of 1.23. For further detail, see table 2.

3.4 Relationship between ventricular width and dynamic cerebellar displacement

For this part of the analysis four patients were excluded as they had been treated with a ventriculoperitoneal shunt for their hydrocephalus, which is expected to influence the FOHR. In fact, all shunt patients were also CM2 patients. Among the 23 CM1 patients left, the FOHR ranged from 0.30 to 0.44 (mean 0.36, SD ± 0.44, see Fig. 13). Eight patients had a FOHR > 0.37 which according to O'Hayon et al. defines hydrocephalus [19]. For further detail about ventricle size, please refer to table 2. As the first part of the analysis showed the greater sensitivity of VIDM compared to VI, all displacements have been evaluated using VIDM. A poor relationship between the FOHR and the extent of the dynamic cerebellar displacement was detected with an adjusted R^2 of -4% and a high p value (>0.05).

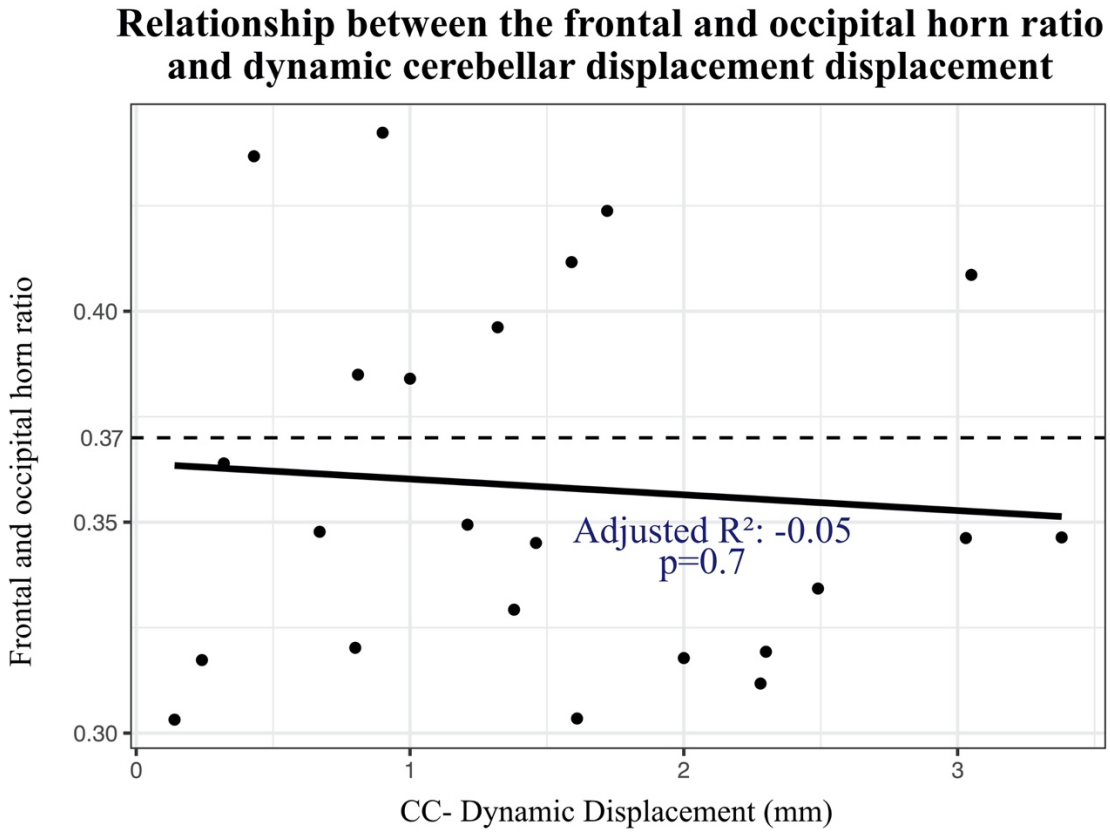

Fig. 13

Fig. 13 Relationship between the frontal occipital horn ratio (FOHR) and dynamic cerebellar displacement. Every point represents one patient without a ventriculoperitoneal shunt (n=23). The dashed line is position at y=0.37 and thus, all patients above the line are hydrocephalic. Regression is shown by the adjusted R^2 and the p-value.

3.5 Comparing the degree of herniation on CINE and conventional, static sequences

In Fig. 14 the distance between cerebellum-CSF interface and the C3-RL is illustrated for each patient. Here, the static sequences are displayed by the purple bars, $CINE_{caudal}$ by the orange and $CINE_{cranial}$ by the blue bars. The C3-RL corresponds to 0 mm on the y-axis. Note that in two cases (patients 3 and 22) the herniated tissue ends caudal to C3-RL, why the distance from C3-RL to the cerebellum-CSF interface becomes negative.

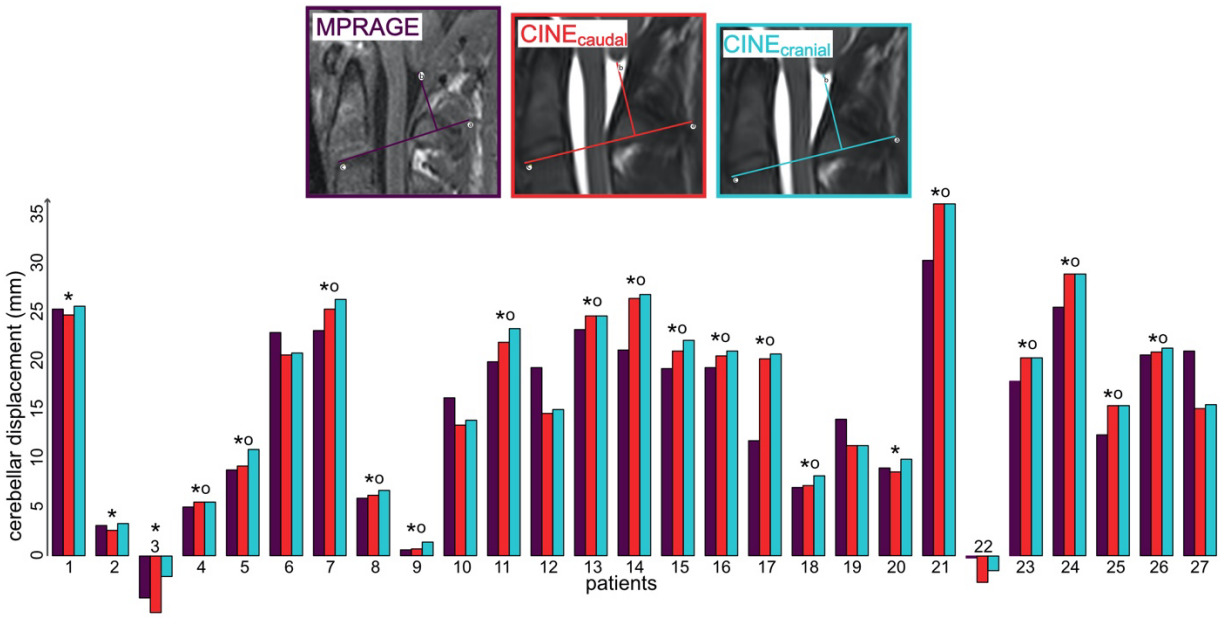

Fig. 14

Fig. 14 Distance from the C3-reference line to the cerebellar-cerebrospinal fluid interface in the static image (purple, furthest left), the most caudal (orange, in the middle) and most cranial (blue, to the right) image in the CINE sequence for every single patient. Patients are marked by an "o" when the distance to the reference line is greater in the $CINE_{cranial}$ than in static image. When the distance from the reference line is greater to the $CINE_{caudal}$ than to the static image, the patient is marked by a "*". Adapted from Fig. 4 in Tietze et al. (24).

In 21/27 cases (78%) the herniation on the static image is greater than on $CINE_{cranial}$ ("*", the purple bar from C3-RL to the interface is shorter than the blue one). In 17/27 cases (63%) the herniation on the static image is greater than the herniation in $CINE_{caudal}$("o", the purple bar from C3-RL to the interface is shorter than the orange one), which are the same cases in which the static herniation is larger than both, the $CINE_{cranial}$ and $CINE_{caudal}$. Hence, in 4 cases (15%) the herniation on the static image is between the herniation in $CINE_{caudal}$ and $CINE_{cranial}$. However, no significant difference in between the extent of herniation was found between the sequences (F-value = 0.12; $p > 0.05$) using ANOVA.

Table 1 summarizes the degree of herniation detected using VI as the distance from the cerebellar-CSF interface to the C3-RL on the static image, $CINE_{cranial}$ and $CINE_{caudal}$.

Table 1: Distances from the reference line to the cerebellar-cerebrospinal fluid- interface on the static image, the most cranial and most caudal image in the CINE sequence.

	Range	Median	Mean	SD
Unit	mm	mm	mm	mm
$MPRAGE_{static}$	0 – 30	18	15	9
$CINE_{cranial}$	1 – 36	16	16	9
$CINE_{caudal}$	0 – 36	15	16	9

Table 2: Type of CM, movement in mm using the voxel intensity distribution method (VIDM) with standard deviation (SD) and visual inspection (VI) in the craniocaudal (CC), anteroposterior (AP) direction, the frontal occipital horn ratio (FOHR) and description of spinal cord pathology, at which height and width of the syringohydromyelia, if present.

Patient ID	Chiari Malformation type	Movement ± SD VIDM (mm)	CC Movement, VI (mm)	AP Movement, VI (mm)	FOHR	Ventriculoperitoneal shunt	Spinal cord pathology
1	1	1.21 ± 0.04	0.9	1.1	0.35	No	No
2	1	2.28 ± 0.18	0.7	0.5	0.31	No	No
3	1	3.38 ± 0.16	3.7	1.8	0.35	No	Edema at C3
4	2	0.67 ± 0.20	0	0	0.48	Yes	Syringohydromyelia at TH6 (7 mm AP)
5	1	2.30 ± 0.12	1.7	0.5	0.32	No	Syringohydromyelia from C3 to TH12 (≥ 2 mm)
6	1	0.8 ± 0.06	0.2	1.6	0.32	No	No
7	1	1.38 ± 0.04	1	0.9	0.33	No	No
8	1	0.32 ± 0.06	0.5	0.6	0.36	No	No
9	1	3.05 ± 0.04	0.7	0.7	0.41	No	No
10	1	0.81 ± 0.14	0.5	-0.5	0.38	No	No
11	1	1.72 ± 0.02	1.4	0.7	0.42	No	No
12	1	2.49 ± 0.39	0.4	-0.4	0.33	No	Edema and cysts from C2 to C4
13	1	0.90 ± 0.05	0	1.1	0.44	No	No
14	1	1.00 ± 0.14	0.4	0.8	0.38	No	No
15	1	3.03 ± 0.38	1.1	1.7	0.35	No	No
16	1	0.24 ± 0.11	0.5	0.4	0.32	No	Syringohydromyelia from C3 to C5 (3 mm)
17	1	1.61 ± 0.05	0.5	1.4	0.30	No	No

18	1	1.32 ± 0.10	1	0.2	0.40	No	No
19	2	0.3 ± 0.67	0	0	0.41	Yes	No
20	1	1.46 ± 0.06	1.3	1.3	0.35	No	No
21	1	0.14 ± 0.11	0	0	0.30	No	No
22	1	1.59 ± 0.24	1.2	0.8	0.41	No	No
23	2	0.41 ± 0.29	0	0	0.45	Yes	No
24	1	0.67 ± 0.17	0	1.3	0.35	No	No
25	2	0.73 ± 0.76	0	0	0.58	Yes	No
26	1	0.43 ± 0.13	0.4	0.7	0.44	No	No
27	1	2.00 ± 0.11	0.4	1.5	0.32	No	No

4 Discussion

4.1 Principal findings and comparison to the state of literature

This study focused on the quantification of tissue movement to improve diagnostic criteria to facilitate assessment on the need for intervention in CM patients. Two aspects were investigated; the correlation of the dynamic cerebellar herniation in patients with CM, associated pathologies arising from CSF flow disturbances and the comparison between conventional, static and dynamic MRI sequences with regard to the degree of herniation. Our results indicate that, first, VIDM increases diagnostic reliability significantly compared to the semi-quantitative method that is usually applied in the clinical context. Second, we observed not only cranio-caudal, but also antero-posterior movement using VI. Third, there was no correlation between the presence of hydrocephalus or syringohydromyelia and, finally, a comparison between the displacement on the static, conventional images and the CINE sequence showed that the results did not show consistency.

The VIDM that was developed as part of this work enabled us to demonstrate very small movements, even on a sub-voxel scale. In fact, we were able to detect motion in significantly more patients which could also better be quantified using the VIDM method compared to VI. However, relatively small displacements of the herniated tissue were found in general. One might argue that these small movements might not have any clinical consequence. Indeed, we found no correlation between the presence of a hydrocephalus and cerebellar displacement in the CINE sequence. This is in accordance with the results by Cousin et al. who analyzed the dynamic displacement of 11 CM1 patients using a pixel shift program [14]. Nevertheless, it is conceivable that intermittent herniation can lead to symptoms, for example during head movements or Valsalva maneuvers. This was not investigated in our study and can therefore not be excluded. It is worth noting that all of our patients provided with a ventriculoperitoneal shunt showed no movement at all, which might suggest that the diversion of CSF together with the relief of the elevated intercranial pressure may decrease the pulsatility dependent motion in these patients.

Interestingly, we found that a substantial number of our patients showed not only movement in the cranio-caudal, but also in the antero-posterior direction. In fact, some of the patients showed only antero-posterior dynamics. The VIDM was only designed to measure cranio-caudally, why this could only be assessed by VI, and it is very likely that VIDM would have detected antero-posterior movement in even more cases.

In clinical routine, the extent of herniation of the cerebellum is mostly analyzed on static, 2D or 3D images, i.e. on the MPRAGE sequence. When comparing the static image to the CINE sequence one might expect that the position of the herniated cerebellar tissue on static images lies between that on $CINE_{cranial}$ and $CINE_{caudal}$. However, in the majority of the cases herniation on the static image was detected to be greater than herniation on the $CINE_{caudal}$ and also greater than on $CINE_{cranial}$. Statistically these findings were not significant. Assuming cerebellar tissue has not changed its location between sequences, these observations might more likely suggest a systematic methodological issue in either the image itself or the method of measurement. One attempted explanation of this observation could be the non-isotropic CINE voxel size ($1 * 1 * 4\ mm^3$) compared to the isotropic voxel size of the MPRAGE ($0.9 * 0.9 * 0.9\ mm^3$). A consequence of the larger, cuboid shaped CINE voxel is the higher probability of finding multiple tissue types within the voxel and thus a greater impact of the partial volume effect. As a result, difficulties arise when trying to determine the exact location of the cerebellum-CSF interface, which leads to considerable error bounds. An attempt to account for this error by artificially increasing the MPRAGE slices thickness and thereby simulating the thicker CINE voxel proved unsuccessful. Alternatively, one could shed light on this problem by decreasing the CINE voxel size. However, this would only be possible by increasing the scanning time drastically, which is difficult to integrate into the clinical routine. This indicates that the method of VI may be prone to uncertainty, but it does not explain the methodological issue of either overestimating the herniation in the static image or underestimating the herniation on the CINE sequence.

4.2 Limitations

4.2.1 Imaging in a single plane

The CINE sequence is a 2D sequence and thus movement can only be observed in one plane. It is possible, however, that cerebellar tissue moves in another plane than the one defined by the radiologist. In fact, after repeating the measurements on neighboring slices in the MPRAGE sequence, we found that herniation can vary > 1 mm from slice to slice. This is in accordance to Tubbs et al., who found that the degree of herniation varies with different imaging planes [11]. It is a limitation that we have to determine the CINE imaging plane a priori without knowing the maximum movement.

4.2.2 Artefacts on the CINE sequence

We had to exclude 9/36 patients due to such artifacts or to overcrowding at the craniocervical junction. In fact, 7 of these 9 excluded patients were CM2 patients of whom the analysis

would have been particularly interesting. Because of this widely accepted limitation, researchers have been trying to improve either technical parameters of the balanced steady state free precision sequences [15] or find other fast imaging methods such as half-Fourier acquired single turbo-spin-echo (HASTE) [27]. Other approaches include radial data sampling combined with different image reconstruction algorithms [28].

4.2.3 Measurement of uncertainties

As described above, the small movements of the cerebellar tissue compared to the relatively large voxel size in the CINE sequence compose a limitation to the method. When measuring in discrete steps, uncertainties are at least the size of the smallest step, even in the absence of noise. It would thus be desirable to take data with smaller voxel sizes but this size needs to be balanced against the need for sufficient intensity in the time-resolved measurements. In order to overcome the voxel size limitation uncertainties, we make use of all collected data by fitting the derivative of a moving intensity edge to a Gaussian profile. It is possible, that the Gaussian curve is not the best to describe all the details in our data. However, the small uncertainties in Fig. 7b indicates that the Gaussian curve fits our data very well.

4.2.4 Interrater discrepancies using visual inspection

Assuming distances less than 1 mm could not objectively be seen in VI, we defined significant movement to be ≥ 1 mm. This was a more arbitrary definition than the 3 SD in VIDM. However, even if this threshold would be decreased to 0.5 mm only 15/27 would show movement, which would still be significantly less than the 22/27 using VIDM. The same is true when decreasing the threshold > 0. Hereby, all patients showed movement as measured by the VIDM method compared to 22/27 cases evaluated by the VI method (combining AP and CC movements). In an attempt to evaluate the reproducibility and uncertainties of the VI method, we tried to compare the difference in distances measured by an experienced neuroradiologist and a medical student. Using Cohen's kappa we found poor interrater agreement (Cohen's kappa and p-value for caudal displacement 0.03 and $p<0.05$ and for cranial displacement 0 with a p-value of 0.69) [29]. In this work, we chose to use all values as measured by one experienced neuroradiologist. This is in accordance to the poor interrater reliability observed by Lawrence et al. in their study [1].

4.2.5 Head position

In all scans, patients were placed in supine position with their necks in some different degrees of extension and flexion. Thus, no conclusion from different head positions can be drawn. It

may well be that respiration, the Valsalva maneuver, standing up or other actions involving different pressure gradients might influence the dynamic cerebellar herniation.

4.2.6 FOHR and FOHWR

We quantified the size of the ventricles using the FOHR because it is simpler and more commonly used also in the clinical setting. The FOHWR would probably have been more exact especially in cases with narrow and assymmetrical ventricles. However, the vast majority of the patients analyzed in this study had symmetrical ventricles.

4.2.7 Ventriculoperitoneal shunt

None of the patients with a ventriculoperitoneal shunt showed movement at all. A limitation to this observation, however, is the small number of patients with a shunt (n=4). We excluded all shunted patients when correlating herniation and hydrocephalus assuming that the shunt prevented the ventricular enlargement. As all patients in the CM2 group had a ventriculoperitoneal shunt, we could only examine the correlation between hydrocephalus and cerebellar displacement in CM1 patients. In fact, previous publications have also only examined CM1 patients, which limits our knowledge about CM2 patients [13,14,16]. Further investigations of larger CM2 cohorts are therefore warranted.

4.3 Future Work

This new, automatic, and quantitative method to assess subtle movement on CINE sequences is easily translatable to other imaging areas. In the central nervous system, fine membranes, adhesions, or cyst walls could be an interesting application. Moreover, the patency of third ventriculostomies might be more reliably evaluated using dynamic sequences [30]. Outside the brain, the diagnostics of fetal motor activity, bowel movement, joint dynamics, and cardiac MRI are only few examples of application fields of CINE MRI, where our quantitative measurement method could be of great value.

To our knowledge, this study is the first to describe cerebellar movement not only in the CC, but also AP direction. Although, we could not show any relationship between the two directions of movement, it is important to investigate this further. As Poretti et al. reports, many symptoms occurring in Chiari patients can be accounted for by the compression of the brainstem and we speculate that the AP direction of movement might be clinically relevant [4]. Overall, AP movement was subtle, but as this was only assessed by VI we are not able to make detailed statements here. We chose to measure the AP movement as the distance between the anterior and posterior position, when the cerebellar tissue was in its extreme CC positions ($CINE_{cranial}$ and $CINE_{caudal}$, respectively). This is, however, not necessarily also the

greatest distance between the most anterior and most posterior point and the pattern of movement might be more complex than anticipated. To investigate this a more advanced VIDM method is going to be developed that allows measurements in any in-plane direction. This work focused on the quantification of tissue movement. The presence and extent of hydrocephalus was investigated in relation to it, but not to clinical symptoms. The development of symptoms and complications in CM1 and CM2 are not investigated further in this study. In view of missing healthy controls, this was not possible nor was it the primary focus. In fact, the onset of symptoms and the occurrence of complications in Chiari patients is complex and is based on much more than only the degree and dynamics of herniation [31]. It would, however, be highly relevant to explore clinical observations in relation to herniation and pulsatility to draw potential therapeutic consequences, such as timely craniocervical decompression or any treatment of hydrocephalus.

4.4 Conclusion

This study has shown that the newly developed VIDM measuring the shift of the pulsatility-dependent tonsillar/vermis displacement in CM1/CM2 patients is superior to VI, which is usually done in the clinical setting. The application field of this tool both in the CNS and outside the brain for real-time CINE MRI is likely to be significant. We found a considerable discrepancy between static, conventional sequences and CINE MRI with regard to the extent of herniation. In our patient cohort, dynamic herniation did not correlate to hydrocephalus or syringohydromyelia so far. Further studies including correlations to clinical observation, MRI in dynamic head positions, and an advanced VIDM are warranted.

5 References

1. Lawrence BJ, Urbizu A, Allen PA, Loth F, Tubbs RS, Bunck AC, Kröger J-R, Rocque BG, Madura C, Chen JA, Luciano MG, Ellenbogen RG, Oshinski JN, Iskandar BJ, Martin BA. Cerebellar tonsil ectopia measurement in type I Chiari malformation patients show poor inter-operator reliability. Fluids Barriers CNS. 2018 Dec 17;15(1):33.

2. Chiari H. Ueber Veranderungen des Kleinhirns, des Pons und der Medulla oblongata infolge von kongenitaler Hydrocephalie des Grosshirns. Denkschr Akad Wiss, Wien. 1895;63:71–116.

3. Haddad FA, Qaisi I, Joudeh N, Dajani H, Jumah F, Elmashala A, Adeeb N, Chern JJ, Tubbs RS. The newer classifications of the chiari malformations with clarifications: An anatomical review. Clinical Anatomy. 2018;31(3):314–22.

4. Poretti A, Boltshauser E, Huisman TAGM. Chiari Malformations and Syringohydromyelia in Children. Seminars in Ultrasound, CT and MRI. 2016 Apr;37(2):129–42.

5. Markunas CA, Tubbs RS, Moftakhar R, Ashley-Koch AE, Gregory SG, Oakes WJ, Speer MC, Iskandar BJ. Clinical, radiological, and genetic similarities between patients with Chiari Type I and Type 0 malformations. J Neurosurg Pediatr. 2012 Apr;9(4):372–8.

6. Ganeriwal V, Dey P, Bawage R, Gore B. Giant meningoencephalocele with Arnold-Chiari type III malformation and anaesthetic challenges: A rare case report. Saudi J Anaesth. 2019;13(2):136–9.

7. Williams H. A unifying hypothesis for hydrocephalus, Chiari malformation, syringomyelia, anencephaly and spina bifida. Cerebrospinal Fluid Res. 2008 Apr 11;5:7.

8. Rekate HL. The definition and classification of hydrocephalus: a personal recommendation to stimulate debate. Cerebrospinal Fluid Res. 2008 Jan 22;5:2.

9. Karimy JK, Duran D, Hu JK, Gavankar C, Gaillard JR, Bayri Y, Rice H, DiLuna ML, Gerzanich V, Simard JM, Kahle KT. Cerebrospinal fluid hypersecretion in pediatric hydrocephalus. Neurosurgical Focus. 2016 Nov 1;41(5):E10.

10. Ganesh D, Sagayaraj BM, Barua RK, Sharma N, Ranga U. Arnold Chiari malformation with spina bifida: a lost opportunity of folic Acid supplementation. J Clin Diagn Res. 2014 Dec;8(12):OD01-03.

11. Tubbs RS, Yan H, Demerdash A, Chern JJ, Fries FN, Oskouian RJ, Oakes WJ. Sagittal MRI often overestimates the degree of cerebellar tonsillar ectopia: a potential for misdiagnosis of the Chiari I malformation. Childs Nerv Syst. 2016 Jul 1;32(7):1245–8.

12. Battal B, Kocaoglu M, Bulakbasi N, Husmen G, Tuba Sanal H, Tayfun C. Cerebrospinal fluid flow imaging by using phase-contrast MR technique. Br J Radiol. 2011 Aug;84(1004):758–65.

13. Radmanesh A, Greenberg JK, Chatterjee A, Smyth MD, Limbrick DD, Sharma A. Tonsillar pulsatility before and after surgical decompression for children with Chiari

malformation type 1: an application for true fast imaging with steady state precession. Neuroradiology. 2015 Apr;57(4):387–93.

14. Cousins J, Haughton V. Motion of the Cerebellar Tonsils in the Foramen Magnum during the Cardiac Cycle. American Journal of Neuroradiology. 2009 Sep 1;30(8):1587–8.

15. Lee H-L, Shankaranarayanan A, Pohost GM, Nayak KS. Improved 3 Tesla Cardiac Cine Imaging using Wideband SSFP. Magn Reson Med. 2010 Jun;63(6):1716–22.

16. Sharma A, Parsons MS, Pilgram TK. Balanced steady-state free-precession MR imaging for measuring pulsatile motion of cerebellar tonsils during the cardiac cycle: a reliability study. Neuroradiology. 2012 Feb;54(2):133–8.

17. Reinard K, Basheer A, Phillips S, Snyder A, Agarwal A, Jafari-Khouzani K, Soltanian-Zadeh H, Schultz L, Aho T, Schwalb JM. Simple and reproducible linear measurements to determine ventricular enlargement in adults. Surg Neurol Int [Internet]. 2015 Apr 9 [cited 2020 Mar 23];6. Available from: https://www.ncbi.nlm.nih.gov/pmc/articles/PMC4399169/

18. Mann S, Wilkinson J, Fourney D, Stoneham G. Comparison of Computed Tomography 3-Dimensional Volumetric Analysis of Ventricular Size to Visual Radiological Assessment. Journal of Computer Assisted Tomography. 2009 Oct;33(5):789–94.

19. O'Hayon BB, Drake JM, Ossip MG, Tuli S, Clarke M. Frontal and Occipital Horn Ratio: A Linear Estimate of Ventricular Size for Multiple Imaging Modalities in Pediatric Hydrocephalus. Pediatr Neurosurg. 1998;29(5):245–9.

20. Jamous M, Sood S, Kumar R, Ham S. Frontal and Occipital Horn Width Ratio for the Evaluation of Small and Asymmetrical Ventricles. PNE. 2003;39(1):17–21.

21. Alperin N, Kulkarni K, Roitberg B, Loth F, Pandian NK, Mafee MF, Foroohar M, Lichtor T. Analysis of magnetic resonance imaging–based blood and cerebrospinal fluid flow measurements in patients with Chiari I malformation: a system approach. Neurosurgical Focus. 2001 Jul 1;11(1):1–10.

22. Massimi L, Frassanito P, Bianchi F, Tamburrini G, Caldarelli M. Bony decompression vs duraplasty for Chiari I malformation: does the eternal dilemma matter? Childs Nerv Syst. 2019 Oct;35(10):1827–38.

23. González Ballester MÁ, Zisserman AP, Brady M. Estimation of the partial volume effect in MRI. Medical Image Analysis. 2002 Dec 1;6(4):389–405.

24. Tietze M, Schaumann A, Thomale U, Hofmann Ph, Tietze A. Dynamic cerebellar herniation in Chiari patients during the cardiac cycle evaluated by dynamic magnetic resonance imaging. Neuroradiology. 2019 Jul;61(7):825–32.

25. Cooper MJ, Nathans R. The resolution function in neutron diffractometry. I. The resolution function of a neutron diffractometer and its application to phonon measurements. Acta Cryst. 1967 Sep 10;23(3):357–67.

26. Business statistics : based on Schaum's outline of theory and problems of business statistics, third edition, by Leonard J. Kazmier [Internet]. New York : McGraw-Hill;

2003 [cited 2020 Apr 29]. 198 p. Available from: http://archive.org/details/businessstatisti0000unse

27. Kulinna-Cosentini C, Czerny C, Baumann A, Weber M, Sinko K. TrueFisp versus HASTE sequences in 3T cine MRI: Evaluation of image quality during phonation in patients with velopharyngeal insufficiency. Eur Radiol. 2016 Sep;26(9):2892–8.

28. Zhang S, Block KT, Frahm J. Magnetic resonance imaging in real time: Advances using radial FLASH. Journal of Magnetic Resonance Imaging. 2010;31(1):101–9.

29. Crewson PE. Reader Agreement Studies. American Journal of Roentgenology. 2005 May 1;184(5):1391–7.

30. Hodel J, Decq P, Rahmouni A, Bastuji-Garin S, Maraval A, Combes C, Jarraya B, Le Guérinel C, Gaston A. Brain ventricular wall movement assessed by a gated cine MR trueFISP sequence in patients treated with endoscopic third ventriculostomy. Eur Radiol. 2009 Jun 19;19(12):2789.

31. Raybaud C, Jallo GI. Chapter 2 - Chiari 1 deformity in children: etiopathogenesis and radiologic diagnosis. In: Manto M, Huisman TAGM, editors. Handbook of Clinical Neurology [Internet]. Elsevier; 2018 [cited 2020 Mar 20]. p. 25–48. (The Cerebellum: Disorders and Treatment; vol. 155). Available from: http://www.sciencedirect.com/science/article/pii/B9780444641892000020

6 Eidesstattliche Versicherung

„Ich, Mia Tietze, versichere an Eides statt durch meine eigenhändige Unterschrift, dass ich die vorgelegte Dissertation mit dem Thema: *Magnetresonanztomographische Untersuchung der Kleinhirntonsillenmotilität bei Chiari Malformationen / Magnetic resonance imaging of dynamic cerebellar herniation in patients with Chiari Malformations* selbstständig und ohne nicht offengelegte Hilfe Dritter verfasst und keine anderen als die angegebenen Quellen und Hilfsmittel genutzt habe.
Alle Stellen, die wörtlich oder dem Sinne nach auf Publikationen oder Vorträgen anderer Autoren/innen beruhen, sind als solche in korrekter Zitierung kenntlich gemacht. Die Abschnitte zu Methodik (insbesondere praktische Arbeiten, Laborbestimmungen, statistische Aufarbeitung) und Resultaten (insbesondere Abbildungen, Graphiken und Tabellen) werden von mir verantwortet.

Ich versichere ferner, dass ich die in Zusammenarbeit mit anderen Personen generierten Daten, Datenauswertungen und Schlussfolgerungen korrekt gekennzeichnet und meinen eigenen Beitrag sowie die Beiträge anderer Personen korrekt kenntlich gemacht habe (siehe Anteilserklärung). Texte oder Textteile, die gemeinsam mit anderen erstellt oder verwendet wurden, habe ich korrekt kenntlich gemacht.

Meine Anteile an etwaigen Publikationen zu dieser Dissertation entsprechen denen, die in der untenstehenden gemeinsamen Erklärung mit dem Erstbetreuer angegeben sind. Für sämtliche im Rahmen der Dissertation entstandenen Publikationen wurden die Richtlinien des ICMJE (International Committee of Medical Journal Editors; www.icmje.og) zur Autorenschaft eingehalten. Ich erkläre ferner, dass ich mich zur Einhaltung der Satzung der Charité – Universitätsmedizin Berlin zur Sicherung Guter Wissenschaftlicher Praxis verpflichte.

Weiterhin versichere ich, dass ich diese Dissertation weder in gleicher noch in ähnlicher Form bereits an einer anderen Fakultät eingereicht habe.

Die Bedeutung dieser eidesstattlichen Versicherung und die strafrechtlichen Folgen einer unwahren eidesstattlichen Versicherung (§§156, 161 des Strafgesetzbuches) sind mir bekannt und bewusst.“

Datum Unterschrift

7 Anteilserklärung

Mia Tietze hatte folgenden Anteil an der folgenden Publikation:

Tietze M, Schaumann A, Thomale U, Hofmann Ph, Tietze A., Dynamic cerebellar herniation in Chiari patients during the cardiac cycle evaluated by dynamic magnetic resonance imaging, Neuroradiology, 2019 Jul;61(7):825–32.

Beitrag im Einzelnen:

- Entwicklung der Fragestellung in Zusammenarbeit mit Prof. U.-W. Thomale
- Planung der Studie in Zusammenarbeit mit Dr. A. Schaumann und Prof. U.-W. Thomale
- Entwicklung der Voxel Intensity Distribution Methode in Zusammenarbeit mit Prof. Dr. Ph. Hofmann
- Selbstständige Befundung der radiologischen Bildgebung (Supervision durch Dr. A. Tietze und Prof. U.-W. Thomale und Dr. A. Schaumann)
- Selbstständig durchgeführte Datenerhebung (Korrekturen durch Prof. U.-W. Thomale, Dr. A. Schaumann, Dr. A. Tietze)
- Selbstständige Durchführung der statistischen Analyse. Daraus sind folgende Tabellen und Graphen entstanden: „Figure" 11, 12, 13 und 14 und „Table" 1 und 2. (Korrekturen durch Prof. U.-W. Thomale und Dr. A. Schaumann)
- Eigenständige Erstellung des Manuskriptes und Literaturrecherche (Korrekturen durch Prof. U.-W. Thomale und Dr. A. Tietze)
- Teilhabe an der Einreichung des Papers und Korrekturen im Review- Verfahren (Federführung des Reviewverfahren Dr. A. Tietze)

Mia Tietze

8 Extraction from journal summary list

Journal Data Filtered By: **Selected JCR Year: 2017** Selected Editions: SCIE,SSCI
Selected Categories: **"RADIOLOGY, NUCLEAR MEDICINE and MEDICAL IMAGING"** Selected Category Scheme: WoS
Gesamtanzahl: 128 Journale

Rank	Full Journal Title	Total Cites	Journal Impact Factor	Eigenfactor Score
1	JACC-Cardiovascular Imaging	8,104	10.247	0.026360
2	European Heart Journal-Cardiovascular Imaging	4,630	8.336	0.020640
3	EUROPEAN JOURNAL OF NUCLEAR MEDICINE AND MOLECULAR IMAGING	14,983	7.704	0.024870
4	RADIOLOGY	54,109	7.469	0.063710
5	JOURNAL OF NUCLEAR MEDICINE	27,101	7.439	0.037560
6	CLINICAL NUCLEAR MEDICINE	4,756	6.281	0.006950
7	INVESTIGATIVE RADIOLOGY	6,486	6.224	0.012410
8	Circulation-Cardiovascular Imaging	5,438	6.221	0.020160
9	IEEE TRANSACTIONS ON MEDICAL IMAGING	17,837	6.131	0.024200
10	ULTRASOUND IN OBSTETRICS & GYNECOLOGY	12,420	5.654	0.018820
11	INTERNATIONAL JOURNAL OF RADIATION ONCOLOGY BIOLOGY PHYSICS	46,595	5.554	0.055060
12	JOURNAL OF CARDIOVASCULAR MAGNETIC RESONANCE	4,918	5.457	0.013530
13	NEUROIMAGE	92,719	5.426	0.152610
14	MEDICAL IMAGE ANALYSIS	6,383	5.356	0.011900
15	RADIOTHERAPY AND ONCOLOGY	17,184	4.942	0.027840
16	HUMAN BRAIN MAPPING	20,334	4.927	0.042810
17	SEMINARS IN NUCLEAR MEDICINE	2,285	4.558	0.002990
18	ULTRASCHALL IN DER MEDIZIN	2,201	4.389	0.004310
19	MAGNETIC RESONANCE IN MEDICINE	31,440	4.082	0.034130
20	EUROPEAN RADIOLOGY	18,615	4.027	0.034120
20	SEMINARS IN RADIATION ONCOLOGY	2,480	4.027	0.003620
22	JOURNAL OF NUCLEAR CARDIOLOGY	3,508	3.847	0.004120
23	AMERICAN JOURNAL OF NEURORADIOLOGY	22,667	3.653	0.029840
24	JOURNAL OF MAGNETIC RESONANCE IMAGING	16,398	3.612	0.027440
25	MOLECULAR IMAGING AND BIOLOGY	2,415	3.608	0.005480

Rank	Full Journal Title	Total Cites	Journal Impact Factor	Eigenfactor Score
26	Biomedical Optics Express	8,120	3.482	0.022750
27	INTERNATIONAL JOURNAL OF HYPERTHERMIA	3,350	3.440	0.004040
28	Journal of the American College of Radiology	3,228	3.383	0.007340
29	RADIOGRAPHICS	11,207	3.249	0.008990
30	AMERICAN JOURNAL OF ROENTGENOLOGY	33,453	3.125	0.031050
31	Journal of Cardiovascular Computed Tomography	1,608	3.095	0.004280
32	KOREAN JOURNAL OF RADIOLOGY	2,331	3.072	0.004670
33	NMR IN BIOMEDICINE	7,537	3.031	0.014150
34	CANCER IMAGING	1,150	3.016	0.002250
35	Contrast Media & Molecular Imaging	1,215	2.934	0.002490
36	MEDICAL PHYSICS	25,701	2.884	0.035220
37	Radiation Oncology	5,157	2.862	0.013540
38	EUROPEAN JOURNAL OF RADIOLOGY	12,571	2.843	0.025400
39	Clinical Neuroradiology	630	2.790	0.002090
40	JOURNAL OF VASCULAR AND INTERVENTIONAL RADIOLOGY	9,021	2.758	0.012460
41	JOURNAL OF NEURORADIOLOGY	949	2.706	0.001620
42	PHYSICS IN MEDICINE AND BIOLOGY	24,912	2.665	0.032160
43	ULTRASOUND IN MEDICINE AND BIOLOGY	10,316	2.645	0.013450
44	EJNMMI Research	1,110	2.630	0.004030
45	MAGNETIC RESONANCE IMAGING	7,194	2.564	0.011680
46	RADIATION RESEARCH	8,468	2.530	0.006760
47	STRAHLENTHERAPIE UND ONKOLOGIE	2,820	2.459	0.004600
48	ABDOMINAL IMAGING	3,203	2.443	0.005940
49	COMPUTERIZED MEDICAL IMAGING AND GRAPHICS	2,190	2.435	0.002730
49	Dose-Response	824	2.435	0.001320
51	ULTRASONICS	6,518	2.377	0.009140
52	QUARTERLY JOURNAL OF NUCLEAR MEDICINE AND MOLECULAR IMAGING	1,032	2.368	0.001450
53	JOURNAL OF BIOMEDICAL OPTICS	13,503	2.367	0.019540
54	NEURORADIOLOGY	5,420	2.346	0.007640
55	ULTRASONIC IMAGING	1,076	2.300	0.000690
56	CLINICAL RADIOLOGY	6,234	2.282	0.008470

Selected JCR Year: 2017; Selected Categories: "RADIOLOGY, NUCLEAR MEDICINE and MEDICAL IMAGING"

Rank	Full Journal Title	Total Cites	Journal Impact Factor	Eigenfactor Score
57	Physica Medica-European Journal of Medical Physics	1,915	2.240	0.005110
58	QUANTITATIVE IMAGING IN MEDICINE AND SURGERY	861	2.231	0.002490
59	Brachytherapy	1,991	2.227	0.004240
60	CARDIOVASCULAR AND INTERVENTIONAL RADIOLOGY	5,429	2.210	0.009530
61	NUCLEAR MEDICINE AND BIOLOGY	3,880	2.203	0.004770
62	Journal of Contemporary Brachytherapy	556	2.146	0.001210
63	Diagnostic and Interventional Imaging	1,127	2.115	0.003010
64	ACADEMIC RADIOLOGY	5,399	2.110	0.009190
65	INTERNATIONAL JOURNAL OF CARDIOVASCULAR IMAGING	2,951	2.036	0.008210
66	JOURNAL OF RADIATION RESEARCH	2,439	2.031	0.004140
67	INTERNATIONAL JOURNAL OF RADIATION BIOLOGY	4,307	1.970	0.003240
68	International Journal of Computer Assisted Radiology and Surgery	2,099	1.961	0.004320
69	JOURNAL OF NEUROIMAGING	1,952	1.953	0.004640
70	Zeitschrift fur Medizinische Physik	519	1.891	0.001450
71	DENTOMAXILLOFACIAL RADIOLOGY	2,617	1.848	0.003500
72	MAGNETIC RESONANCE MATERIALS IN PHYSICS BIOLOGY AND MEDICINE	1,473	1.832	0.003150
73	PEDIATRIC RADIOLOGY	6,350	1.826	0.008180
74	ACTA RADIOLOGICA	4,304	1.823	0.006360
75	Radiologia Medica	2,001	1.819	0.003590
76	BRITISH JOURNAL OF RADIOLOGY	8,804	1.814	0.013010
77	Magnetic Resonance Imaging Clinics of North America	931	1.740	0.001780
78	Radiology and Oncology	706	1.722	0.001390
79	RADIOLOGIC CLINICS OF NORTH AMERICA	2,441	1.695	0.002180
80	CANCER BIOTHERAPY AND RADIOPHARMACEUTICALS	1,619	1.682	0.001850
81	ANNALS OF NUCLEAR MEDICINE	2,133	1.656	0.003120

Selected JCR Year: 2017; Selected Categories: "RADIOLOGY, NUCLEAR MEDICINE and MEDICAL IMAGING"

Rank	Full Journal Title	Total Cites	Journal Impact Factor	Eigenfactor Score
82	ROFO-FORTSCHRITTE AUF DEM GEBIET DER RONTGENSTRAHLEN UND DER BILDGEBENDEN VERFAHREN	1,462	1.636	0.002200
83	BMC MEDICAL IMAGING	815	1.635	0.001690
84	JOURNAL OF THORACIC IMAGING	1,311	1.624	0.002200
85	Diagnostic and Interventional Radiology	1,164	1.618	0.002300
86	SKELETAL RADIOLOGY	5,482	1.567	0.007550
87	JOURNAL OF DIGITAL IMAGING	1,680	1.536	0.002750
88	JOURNAL OF ULTRASOUND IN MEDICINE	6,500	1.530	0.008700
89	RADIATION AND ENVIRONMENTAL BIOPHYSICS	1,362	1.527	0.001740
90	SEMINARS IN MUSCULOSKELETAL RADIOLOGY	802	1.521	0.001310
91	Medical Ultrasonography	739	1.512	0.001750
92	Abdominal Radiology	533	1.506	0.001220
93	NUCLEAR MEDICINE COMMUNICATIONS	2,848	1.495	0.004230
94	Journal of Medical Imaging and Radiation Oncology	1,113	1.478	0.002660
95	Magnetic Resonance in Medical Sciences	649	1.455	0.001320
96	Molecular Imaging	1,134	1.414	0.001610
97	NUKLEARMEDIZIN-NUCLEAR MEDICINE	600	1.352	0.000760
98	Journal of Applied Clinical Medical Physics	2,182	1.301	0.005370
99	JOURNAL OF COMPUTER ASSISTED TOMOGRAPHY	5,296	1.292	0.004040
100	NEUROIMAGING CLINICS OF NORTH AMERICA	1,102	1.275	0.001260
101	JOURNAL OF RADIOLOGICAL PROTECTION	984	1.274	0.002030
102	Revista Espanola de Medicina Nuclear e Imagen Molecular	435	1.202	0.000880
103	Journal of Innovative Optical Health Sciences	418	1.136	0.000640
104	Cancer Radiotherapie	812	1.128	0.001010
105	APPLIED RADIATION AND ISOTOPES	7,237	1.123	0.009390
106	SEMINARS IN ULTRASOUND CT AND MRI	871	1.062	0.001110

Selected JCR Year: 2017; Selected Categories: "RADIOLOGY, NUCLEAR MEDICINE and MEDICAL IMAGING"

Rank	Full Journal Title	Total Cites	Journal Impact Factor	Eigenfactor Score
107	Japanese Journal of Radiology	844	1.044	0.002060
108	INTERVENTIONAL NEURORADIOLOGY	1,027	1.021	0.001950
108	Ultrasound Quarterly	499	1.021	0.000720
110	CLINICAL IMAGING	1,911	1.014	0.003510
111	Hellenic Journal of Nuclear Medicine	410	1.008	0.000600
112	SURGICAL AND RADIOLOGIC ANATOMY	2,940	1.003	0.003150
113	CANADIAN ASSOCIATION OF RADIOLOGISTS JOURNAL-JOURNAL DE L ASSOCIATION CANADIENNE DES RADIOLOGISTES	508	1.000	0.000980
114	HEALTH PHYSICS	3,981	0.993	0.003220
115	JOURNAL OF CLINICAL ULTRASOUND	2,101	0.978	0.001870
116	SEMINARS IN INTERVENTIONAL RADIOLOGY	1,054	0.971	0.001420
117	Medical Dosimetry	725	0.886	0.001100
118	RADIATION PROTECTION DOSIMETRY	5,823	0.822	0.006310
119	Journal of Medical Ultrasonics	342	0.677	0.000660
120	International Journal of Radiation Research	132	0.594	0.000270
121	Journal of Medical Imaging and Health Informatics	507	0.549	0.000970
122	Iranian Journal of Radiology	259	0.524	0.000710
123	SEMINARS IN ROENTGENOLOGY	417	0.429	0.000380
124	RADIOLOGE	558	0.376	0.000480
125	Current Medical Imaging Reviews	303	0.299	0.000380
126	Journal of the Belgian Society of Radiology	24	0.270	0.000050
127	RADIOPROTECTION	260	0.225	0.000240
128	JBR-BTR	239	0.195	0.000350

9 Publication

Tietze M, Schaumann A, Thomale U, Hofmann Ph, Tietze A. Dynamic cerebellar herniation in Chiari patients during the cardiac cycle evaluated by dynamic magnetic resonance imaging. Neuroradiology. 2019 Jul;61(7):825–32.

DOI: https://doi.org/10.1007/s00234-019-02203-2

10 Lebenslauf

Mein Lebenslauf wird aus datenschutzrechtlichen Gründen in der elektronischen Version meiner Arbeit nicht veröffentlicht.

11 Komplette Publikationsliste

Tietze M, Schaumann A, Thomale U, Hofmann Ph, Tietze A. Dynamic cerebellar herniation in Chiari patients during the cardiac cycle evaluated by dynamic magnetic resonance imaging. Neuroradiology. 2019 Jul;61(7):825–32.

12 Danksagung

Ich möchte in erster Linie meinem Betreuer, Prof. Dr. Ulrich-Wilhelm Thomale, für die Möglichkeit der Promotion danken. Seit meiner Hausarbeit hat er mir stets mit wertvollen Ratschlägen geholfen und mich viel über das wissenschaftliche Arbeiten gelehrt. Danke auch an Dr. Andreas Schaumann für die fortwährende Unterstützung.

Ein großer Dank geht auch an meine Familie und meine Freunde, die immer für mich da sind.